



Inverse wheel–rail contact force and crossing irregularity identification from measured sleeper accelerations – A model-based Green's function

Downloaded from: <https://research.chalmers.se>, 2025-12-04 10:15 UTC

Citation for the original published paper (version of record):

Milosevic, M., Pålsson, B., Nissen, A. et al (2024). Inverse wheel–rail contact force and crossing irregularity identification from measured sleeper accelerations – A model-based Green's function approach. *Journal of Sound and Vibration*, 589. <http://dx.doi.org/10.1016/j.jsv.2024.118599>

N.B. When citing this work, cite the original published paper.



Inverse wheel–rail contact force and crossing irregularity identification from measured sleeper accelerations – A model-based Green’s function approach

Marko D.G. Milošević^{a,*}, Björn A. Pålsson^a, Arne Nissen^b, Jens C.O. Nielsen^a, Håkan Johansson^a

^a Chalmers University of Technology, Department of Mechanics and Maritime Sciences / CHARMEC SE-412 96, Göteborg, Sweden

^b The Swedish Transport Administration, Box 809 SE-971 25, Luleå, Sweden

ARTICLE INFO

Keywords:

Green’s kernel function method
Inverse problem
Force identification
Irregularity identification
Railway crossing
Condition monitoring

ABSTRACT

A novel model-based method for railway Crossing Panel Condition Monitoring (CPCM) is presented. Based on sleeper accelerations measured during wheel crossing transitions and knowledge of the crossing panel design, it is shown that it is possible to identify the ballast stiffness properties, vertical wheel–rail contact forces and vertical relative wheel–rail displacement trajectories (crossing irregularities) in the crossing panel. The method uses a multibody dynamics simulation model with a finite element representation of the track structure for evaluation of the dynamic interaction between vehicle and crossing panel. Considering the low-frequency domain where the sleeper response is not significantly affected by the influence of the irregularity due to the designed (and current state of the) crossing and wing rail geometry, the ballast condition is identified via a calibration of the distribution of ballast stiffness in the finite element model. This enables ballast stiffness identification without a priori knowledge of the crossing geometry. From the reconstructed track displacements, the wheel–rail contact forces are identified by solving an inverse problem formulated using the Green’s Kernel Function Method (GKFM) that provides a direct link between the track excitation forces and the track response. Further, the irregularity induced by the crossing and wing rail geometry is estimated by taking the difference between the wheel and rail displacements during the crossing transition computed from the identified wheel–rail contact forces. By monitoring the evolving irregularity, the degradation of the crossing rails over time can be assessed. The method is verified and validated using concurrently measured sleeper accelerations and laser scanned crossing geometries from six crossing panels in situ.

1. Introduction

The components in a railway network that enable trains to switch from one track to another are called switches & crossings (S&Cs, turnout). Due to the load-inducing rail discontinuities in the switch and crossing panels, S&Cs experience higher degradation rates and maintenance costs compared to regular plain line tracks. Overall it is estimated that there are over 300,000 S&Cs in the EU 27 countries and that the maintenance cost per S&C is equivalent to that of approximately 0.3 km of plain line track [1]. The annual maintenance

* Corresponding author.

E-mail address: marko.milosevic@chalmers.se (M.D.G. Milošević).

cost for the around 12,000 S&Cs in Sweden has been estimated to be 400 – 450 MSEK ($\sim 40 - 45$ MEUR) [2]. These high maintenance costs create a business case for railway managers to employ condition monitoring solutions for S&Cs that could improve maintenance planning and reduce costs. This paper is focused on the crossing panel and the condition monitoring of crossing geometry and ballast stiffness, see Fig. 1.

The current practice for crossing panel monitoring is by manual inspections in track using measurement templates and visual inspection. These inspections can be complemented with data from track recording cars. An alternative solution that has surfaced in recent years is to monitor the track response that follows from the wheel–crossing transition by using embedded accelerometers mounted on the sleeper adjacent to the crossing transition. The benefits of this solution are that it allows for continuous monitoring and that the assessment is based on the dynamic response of the structure under traffic loading instead of the system at rest. The challenge that remains, however, is to link the measured accelerations to the physical state of the asset.

Previous studies have presented a clear correlation between crossing geometry degradation and increased rail and sleeper accelerations. For example, Ref. [3] reported that accelerations measured in a damaged crossing were on average 70 % higher compared to a crossing geometry where the running surface had recently been repaired. Previous studies based on simulations have also presented a clear correlation between crossing geometry, wheel–rail contact force and track response [4,5]. At least three studies, [6–8], have contrasted measured accelerations at the crossing transition to simulation results. Additional studies on the simulation of dynamic vehicle track-interaction during the crossing transition can be found in [9–11].

Further, several studies used only experimental data processing to characterize the magnitude and frequency contents of the crossing rail accelerations. In [3,7] peak values were used, in [6] spectrograms were used, and in [12] a wavelet transform was used. Ref. [13] proposed a separation of the measured track response into quasi-static and dynamic domains based on deformation wavelength regions to monitor the ballast condition and crossing geometry, respectively, and ref. [14] derived a crossing condition indicator based on a band-passed track response signal between frequencies corresponding to the dynamic domain track deformation wavelengths. It is, therefore, established that a change in crossing geometry condition will lead to a change in track response and that this can be used for condition monitoring purposes.

The ambition behind this paper has been to go beyond indirect condition indicators and quantify the ballast and crossing condition in explicit terms. To this end, this paper develops a Crossing Panel Condition Monitoring (CPCM) method that identifies the ballast stiffness, vertical wheel–rail contact forces and crossing geometry in a crossing panel from measured sleeper accelerations. It uses a multibody simulation model with a structural (FEM) track model to create the physics-informed link between input and output, and a Green's function approach for the inverse load identification.

The CPCM method has been developed using concurrently measured sleeper acceleration data and laser-scanned crossing geometries from six crossing panels on the southern mainline in Sweden. The laser-scanned crossing geometries have allowed for validation of the developed method in the sense that the reconstructed sleeper displacements have been compared to the simulated counterparts with known crossing geometry excitation. An overview of the method is presented in the following section followed by separate sections on the details of each step.

The presented developments are part of a larger effort to develop a model-based numerical procedure that can not only identify but also predict the structural condition of an S&C via embedded sensors. The target system can be described as a Digital Twin representation of the physical system where simulation models, condition monitoring data, and maintenance history are combined to predict and identify the maintenance needs for the S&C on a real-time (or day-to-day) basis in railway operations.

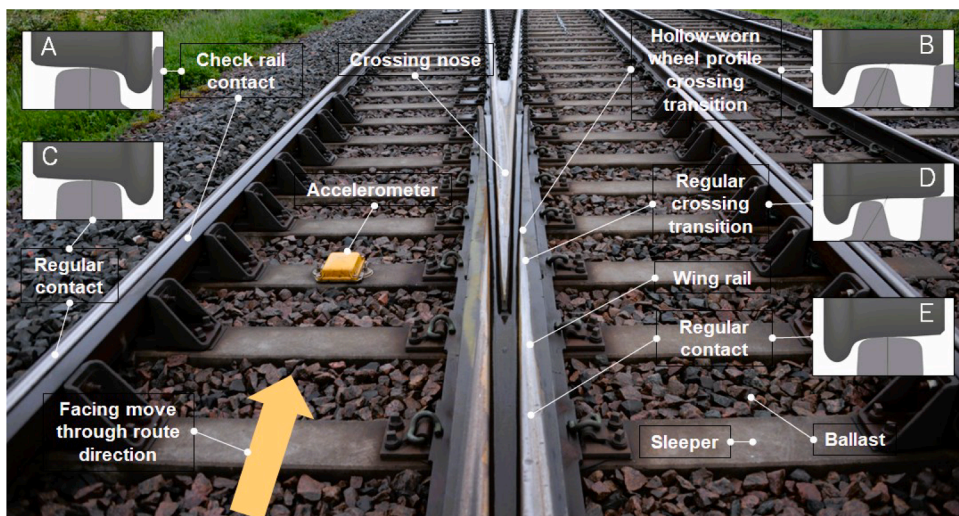


Fig. 1. Illustration of a wheelset transition through the crossing panel with the nomenclature for the main components and wheel–rail contact states. More details concerning this transition can be found in [14].

1.1. Method overview

A flowchart of the Crossing Panel Condition Monitoring (CPCM) scheme is presented in Fig. 2. It uses measured sleeper accelerations and S&C type as inputs. The accelerations are reconstructed to displacements using the technique developed in [13] that is based on frequency domain integration and optimization of the high-pass frequency for baseline distortion detrending. In the third step, a multibody simulation model with a FEM structural track model is generated based on knowledge of the nominal parameters for the S&C (radius, rail fastening stiffness, etc.). The ballast stiffness properties in the model are then calibrated by minimizing the difference between the measured and simulated sleeper displacements during a bogie passage. The calibration is performed using the method developed in [15] with the difference that low-pass filtered track displacement signals are used. This is to separate the quasi-static global deformation pattern of the track from the dynamic response caused by the current state of the crossing geometry, and to allow for ballast stiffness calibration without knowledge of the crossing geometry. In the fourth step, the vertical wheel–rail contact forces at the crossing transition are identified from the reconstructed vertical sleeper displacements using GKFM [16–20], where the unit impulse responses of the track structure (Green's functions) are used to formulate the relationship between the input force and output sleeper displacement, and by solving the inverse problem to obtain force from displacement. Background on the use of GKFM in track modelling and inverse problems is elaborated further in the coming section. Based on the estimated wheel–rail contact forces, the wheel and rail displacements during the crossing transition can be computed in the fifth step. In the final step, the relative vertical wheel–rail trajectory, or crossing irregularity for short, that the wheel experiences as it rolls over the crossing transition is computed by taking the difference between the vertical wheel and rail displacements. The crossing irregularity is studied in a band-pass filtered frequency region as there is too much error and drift in the reconstructed wheel trajectory at low frequencies. Thus, the method outputs ballast stiffness, wheel–rail contact forces and crossing irregularities as condition indicators. By monitoring the evolving indicators, the degradation of the crossing panel over time can be assessed.

1.2. Review on railway track modelling and inverse load identification using Green's functions

A wide range of applications of Green's functions and an extensive use of this method for solving railway dynamics problems can be found in the literature. In [21], a method based on moving Green's functions was employed to solve the dynamic wheel–rail interaction for high-speed trains. In [22], the Green's function method was utilized to calculate the vertical responses of a concrete slab due to a moving train vehicle, showing results from FEM and the Green's function method with a high level of agreement. In [23], a 2.5D FE

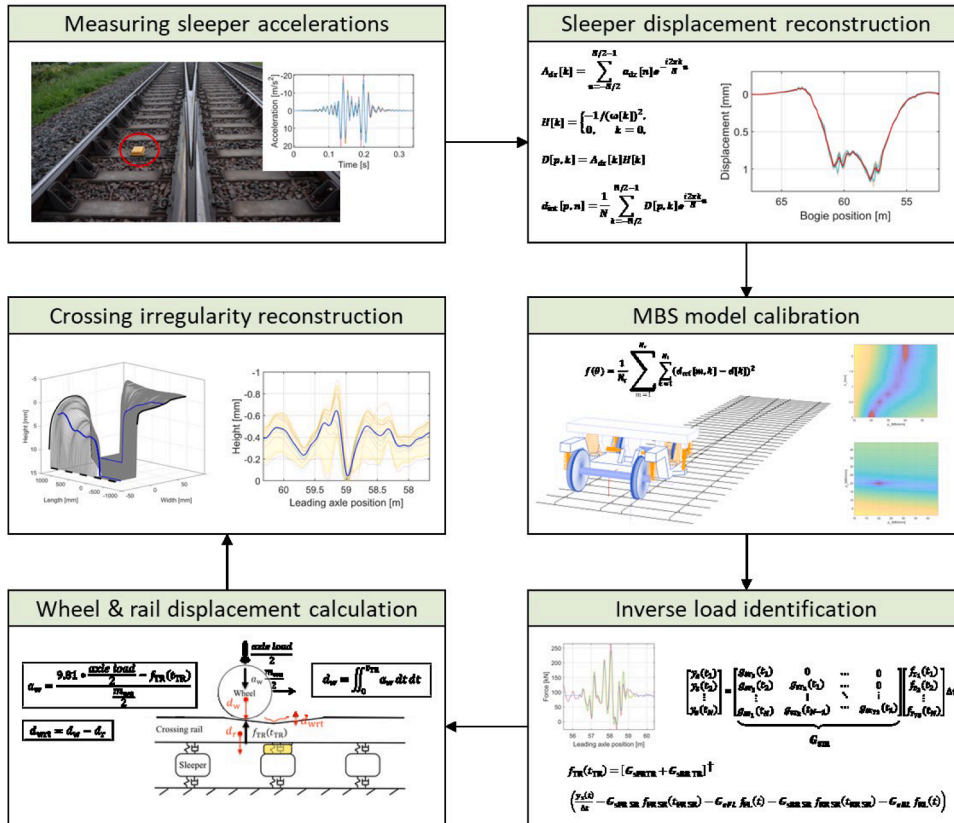


Fig. 2. Workflow from measured sleeper accelerations to identified ballast stiffness, contact forces and crossing irregularity profile.

framework with Green's functions was numerically investigated and experimentally validated for the case of ground vibration induced by Maglev trains running inside a tunnel. In [24], a 3D numerical FE model of a railway track was coupled to a Green's function BEM model of the ground. Good agreement between measured and simulated track velocities (and displacements) was observed. In general, frequent applications of Green's functions in railway mechanics-related problems concern the coupling of a FE model for the track superstructure with a Green's function BEM model for the substructure (ground), see e.g. [24–26].

Overall, in a theoretical background context, Ref. [27] shows the use of Green's functions to solve responses of infinite periodic structures subjected to moving loads, while the PhD thesis [28] addresses time-domain modelling of high-frequency wheel–rail interaction and noise mitigation with detailed derivations of Green's function concepts.

More closely related to the context of the present paper, Refs. [29–31] deal with moving load identification for continuous systems using modal superposition and a convolution integral. Concerning discretized systems and moving load identification, Ref. [32] solves a problem based on a stochastic FE model, while Ref. [33] formulates an explicit form of the Newmark- β method with numerical and experimental load identification assessment. Mostly, the literature on moving load identification is related to bridge structures. Concerning load identification with the GKFM, Refs. [16–20] concern the identification of fixed-point forces instead of moving loads.

Apart from the more conventional approaches for solving the inverse force identification problem in structural dynamics, Ref. [34] uses an augmented Kalman filter for force identification, Ref. [35] applies state-space force identification based on Markov parameters, while Ref. [36] transforms the conventional implicit Newmark- β algorithm into an explicit form. Also, in recent years, machine learning has been employed to solve inverse force identification problems. For example, Refs. [37,38] employ multi-layer perception (MLP) networks for impact force identification for smart composite and electric vehicle battery packs, respectively, while Ref. [39] uses a recurrent neural network (RNN) for impact load identification of nonlinear structures. Reviews on dynamic load identification for mechanical systems and force reconstruction techniques can be found in Refs. [40,41]. A tutorial for moving load dynamic problems is presented in Ref. [42].

Overall, force reconstruction analysis is based on the regularization of a deconvolution problem [43]. Deconvolution or the formulated transfer matrix inversion for force identification is a well-known ill-posed problem. It is usually pseudo-inverted with singular value decomposition (SVD) in regular, generalized [31,43], or truncated form [18,31], and regularized with the Tikhonov regularization method. In this paper, SVD is used for the inverse problem and a low-pass brick digital filter for the regularization. This avoids the dependence of the solution from a regularization parameter, and physically interprets the ill-posedness based on the frequency spectrum of the signal that is being transferred to the forces. No literature has been found for moving load identification using the Green's Kernel Function Method.

2. Instrumentation and field data

The instrumentation concept used for the present study is: (I) an accelerometer mounted on the sleeper next to the crossing transition, as shown in Fig. 1, and (II) a portable 3D laser scanner for scanning rail surface geometry, see Fig. 4. The acceleration sensors that were provided by Konux GmbH were installed in the Swedish railway network as part of Trafikverket's (the Swedish Transport Administration's) research activities on remote condition monitoring of crossing panels initiated in the EU-funded In2Rail project [44]. More details on the characteristics of both sensors can be found in [13].

The two types of measurements were acquired for six crossing panels and are concurrent in time (monitoring period of seven days in

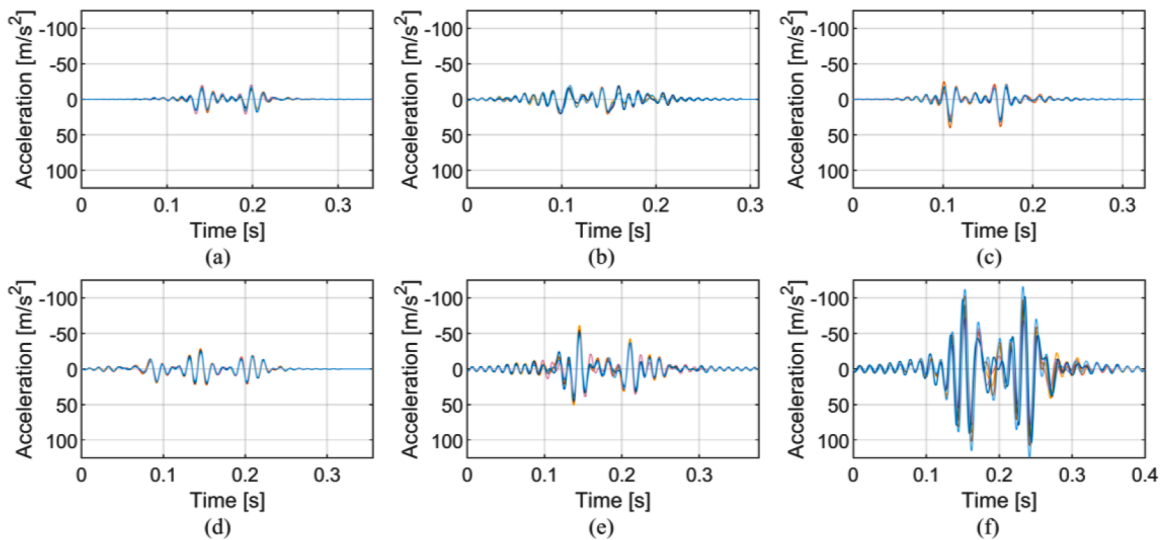


Fig. 3. Examples of sleeper acceleration recordings (five per crossing) chosen with random selection from processed recordings to show the variability of traces for a single crossing: Ho 21B (a), Ho 22A (b), Sg 21A (c), Sg 21B (d), Vad 102 (e), Vad 131 (f). Positive acceleration direction is downwards into the track.

June 2019). The six crossing panels are situated at three locations on the southern mainline in Sweden: Höör, Stehag, and Vätteryd. In this paper, they are labelled with their network IDs as Ho 21B and Ho 22A for Höör, Sg 21A and Sg 21B for Stehag, and Vad 102 and Vad 131 for Vätteryd. The designs of the crossing panels differ among the locations. At Höör, the 60E design is installed featuring rail fastenings with a soft resilient element (rail pad), while Stehag and Vätteryd feature the UIC60 design with a direct and very stiff connection between the crossing rail and sleepers. All S&C have a radius of 1200 metres.

2.1. Acceleration data

The sleeper acceleration data used in this study include 600 cases of X2 passenger trains passing through the six crossing panels (100 cases per panel). As described in [13], the acceleration data was analysed to (I) reconstruct velocity and displacement signals, and (II) determine the train speed. The acceleration signals were recorded at a sampling rate of 2 kHz and low-pass filtered at 250 Hz, which captures the frequency range where the ballast stiffness influence the track response [14]. Examples of low-pass filtered acceleration traces for each crossing panel are shown in Fig. 3. The acceleration levels vary because of differences in design, train speed and crossing condition. Lower sleeper acceleration magnitudes are expected for Ho 21B and Ho 22A due to the softer rail fastening used in these S&C [14].

2.2. Geometry data

The geometry of the crossing and wing rails was measured using the high-precision Creaform HandySCAN 3D laser scanner, see Fig. 4. During the in-situ scanning, additional reference objects were mounted on the crossing rail to increase the quality of the scan. The six scanned and post-processed crossing rail geometries are shown in Fig. 5. The crossing geometry deterioration can be inferred from the dotted lines that represent the intersection between vertical planes and the crossing geometry along typical contact paths on the crossing and wing rails. Based on the straight intersection lines, it is concluded that Ho 21B shows very little geometry change from the nominal profile, while the undulating intersection lines for Vad 131 indicate large amounts of geometry change due to wear and plastic deformation. Additional details concerning geometry processing and the preparation of 2D profiles for the MBS analysis can be found in [14].

3. Model for simulation of dynamic train–track interaction

The dynamic interaction between vehicle and crossing panel is modelled and simulated using multibody simulations (MBS). The analyses are performed with the commercial software Simpack. The track model is a finite element model with all the rails and sleepers modelled by Timoshenko beam elements. All individual rails and sleepers are condensed into super elements using a Craig-Bampton reduction. Each sleeper is supported by a discretized system of independent bushings in the vertical direction that represents the distribution of stiffness and viscous damping of the ballast and subgrade (Winkler bed). Each connection between sleeper and rail is modelled by a single bushing element representing the rail fastening. The degrees-of-freedom for the nodes of the rails and sleepers are partially constrained to reduce the size of the model. Only the vertical displacement is considered for the sleeper nodes, while lateral and vertical displacements and their corresponding rotations are considered for the rail nodes. The model is generated with a S&C model generation script [44] and implemented in Simpack using its non-linear flextrack functionality. It has been verified that a track model length of 37 sleepers is sufficient to simulate the dynamic vehicle–track interaction and that a longer track model does not

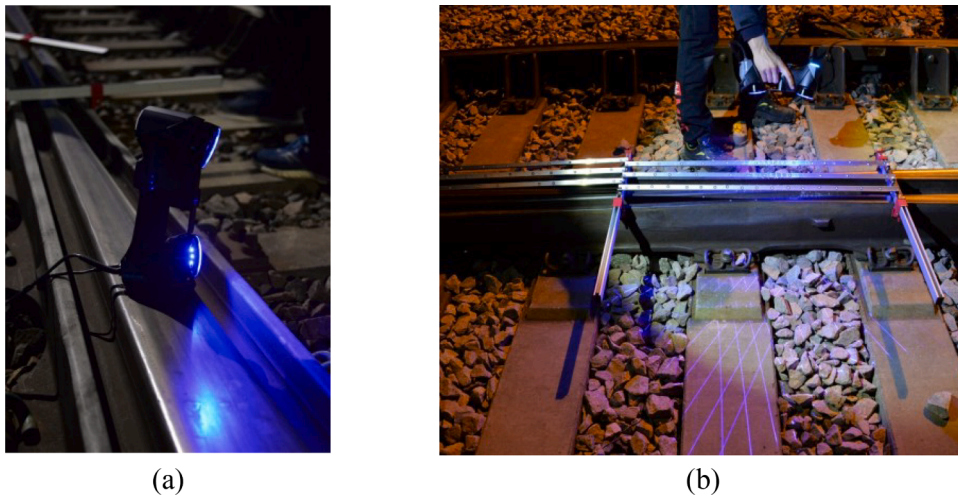


Fig. 4. 3D geometry scan of a crossing transition with a laser scanner (a). To improve scan quality, reference objects with reflective dots were installed (b).

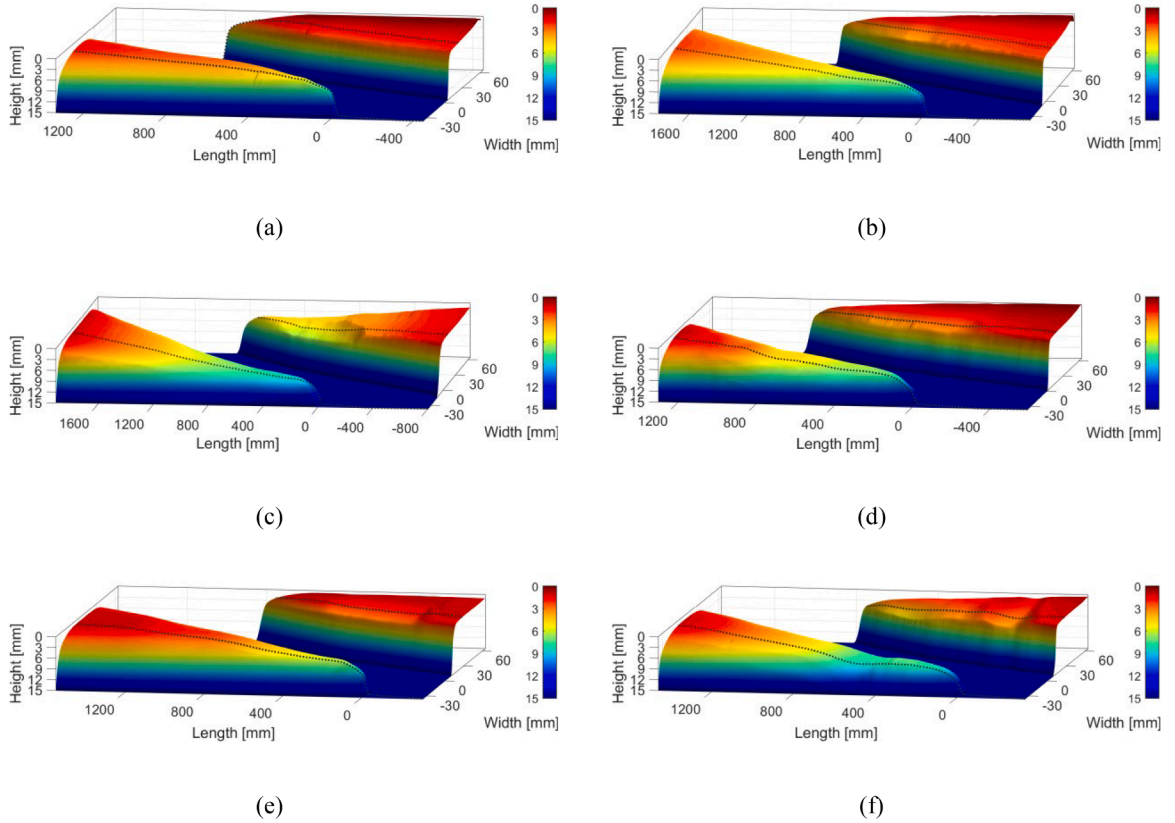


Fig. 5. Crossing rail 3D scans for Ho 21B (a), Ho 22A (b), Sg 21A (c), Sg 21B (d), Vad 102 (e) and Vad 131 (f). The crossing nose (CN) is to the left and the wing rail (WR) is to the right. Dotted lines illustrate a possible wheel path and emphasize the condition of the crossing geometry. The start of the crossing nose is at a longitudinal length position of 0 mm.

change the results at the crossing significantly [13].

The crossing rail geometry is implemented into Simpack by 2D profiles with a 10 mm spacing discretized from the 3D scans of the crossing rail. The software builds a 3D rail geometry from the 2D sections via a cubic spline interpolation. An equivalent linearised Hertz contact is used for the normal wheel–rail contact, while FASTSIM [45] is used to model the tangential contact. The 3D and 2D views of the vehicle–track model are shown in Fig. 6 and model parameters are given in Table 1.

3.1. Calibration of ballast stiffness

This section presents the procedure for the MBS model ballast parameters calibration that is performed for each analyzed crossing panel and is the third step of the CPCM scheme. The calibration is performed to 1) diagnose the ballast conditions, and 2) obtain track

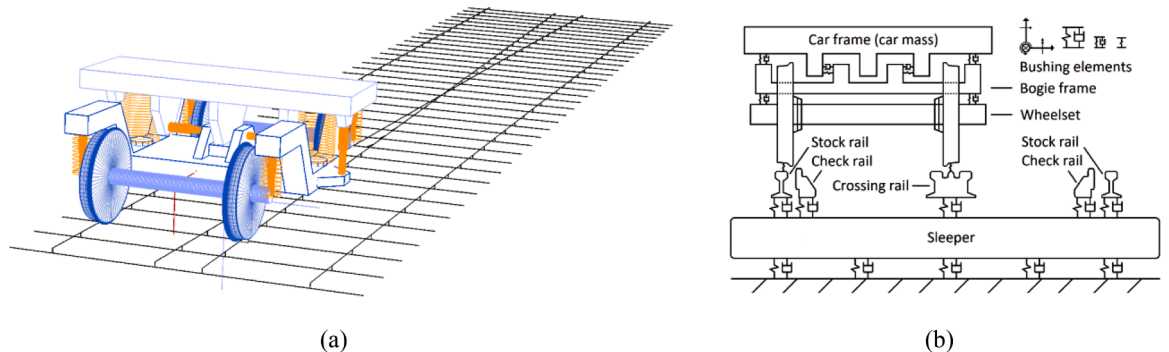


Fig. 6. (a) MBS model of vehicle–track system, and (b) 2D representation of vehicle–track system during passage through the crossing panel.

Table 1

Nominal MBS parameter values with vehicle parameters that correspond to an X2 train cabin car bogie.

MBS model components		Value
Vehicle	Type	Single bogie [46]
	Wheel radius	0.46 m
	Wheelset mass	1340 kg
	Axle load	15500 kg
	Axle spacing	2.9 m
Rail*	Element type	Timoshenko beam
	Lengthwise node spacing	0.3 m
	Profile	60E/UIC60
	Young's modulus	210 GPa
	Mass density	60 kg per metre
	* The equivalent cross-section of crossing nose and wing rails is modelled as having three times the bending stiffness and mass of a standard 60E1 rail.	
Rail pads	Element type	Kelvin bushing
	Vertical stiffness	1200 MN/m (for UIC60)
	Vertical damping	60 MN/m (for 60E)
		25 kNs/m (for UIC60)
Sleeper	Element type	Timoshenko beam
	Lengthwise node spacing	0.25 m average
	Young's modulus	30 GPa
	Mass density	2400 kg/m ³
Ballast	Element type	Kelvin bushings
	Vertical stiffness	30 (MN/m)/m
	Vertical damping	125 (kNs/m)/m

model parameters for the subsequent Green's functions generation and inverse load identification. The calibration method is the same as the one developed in [15] with the difference that only the quasi-static track deflection under a bogie passage is used here for the calibration.

The ballast support stiffness under each sleeper is modelled using linear bushing elements. Possibly voided sleepers (or a more compacted sleeper region) are accounted for by introducing a variation in the ballast stiffness distribution along the crossing panel [15]. A bi-linear ballast model with constant stiffness and a variation in sleeper voids along the crossing transition was considered in [15]. However, in the scope of the used dataset of six crossing panels, the linear ballast model outperformed the bi-linear voided ballast model in terms of calibration fit and parameter sensitivity and is therefore used in the present study.

The stiffness distribution is parameterized using three parameters as illustrated in Fig. 7. The three parameters prescribe the ballast stiffness and its distribution in a region of ± 2 sleepers from the crossing sleeper location. Parameters p_1 and p_2 are outer and inner peak stiffness values in the ± 2 sleeper region, while p_3 is a parameter prescribing the shape of the quadratic distribution of stiffnesses between p_1 and p_2 . (for distribution equations see [15]). It is assumed that the distribution of ballast stiffness is uniform along the length of each sleeper in the lateral track direction.

For calibration, the three ballast parameters are gathered in the vector θ . The calibration objective function is based on the discrepancy between sleeper displacement at the sensor location (crossing sleeper) for the measured (\mathbf{d}_{mea}) and simulated (\mathbf{d}_{sim}) sleeper displacement responses. The objective function $f(\theta)$ that is accounting for N_r measured reference signals with index m of length

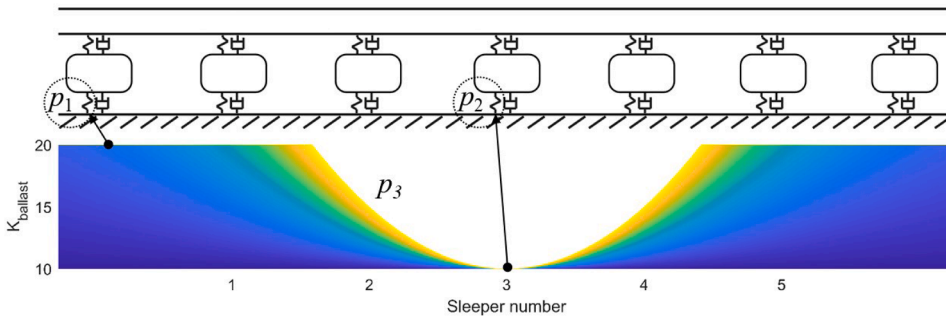


Fig. 7. Three-parameter ballast stiffness distribution model used for model calibration: p_1 outer ballast stiffness, p_2 inner ballast stiffness (corresponding to stiffness at the instrumented crossing sleeper), p_3 quadratic ballast stiffness distribution in the region of ± 2 sleepers from the crossing sleeper.

N_l is presented in Eq. (1).

$$f(\theta) = \frac{1}{N_r} \sum_{m=1}^{N_r} \sum_{k=1}^{N_l} (\mathbf{d}_{\text{mea}}^m(\mathbf{k}) - \mathbf{d}_{\text{sim}}^\theta(\mathbf{k}))^2 \quad (1)$$

Each signal corresponds to a single bogie passage over the crossing. The signal vectors are of length N_l and are synchronized to make a direct overlap of the axle passages in time between measurement and simulation. The ballast stiffness distribution is found by minimizing $f(\theta)$ using a gradient-based optimization algorithm. The ballast stiffness distributions for the six crossing panels found in [15], using the same acceleration and crossing geometry data as in this paper, are presented in Fig. 8. It can be observed that there is a large difference between the crossings in the resulting stiffness distributions. In particular, Vad 131 is an outlier with zero stiffness at the crossing transition (sleeper 17) indicating voided sleeper conditions under the crossing.

For each crossing panel, the calculated sleeper displacements in Fig. 9 were obtained by using the known laser-scanned crossing geometries implemented in the simulation model. In a real condition monitoring situation, however, the crossing geometry will not be known a priori. To circumvent this problem, the calibration in the CPCPM is performed using sleeper displacements corresponding to the track deflection under a constant moving load to exclude the influence from the dynamic excitation generated by the discontinuity in the crossing rails. In the simulations, this reference signal $\mathbf{d}_{\text{sim}, 60\text{E}}$ is obtained by simulating a passage through the crossing panel where the crossing geometry has been replaced by a constant 60E rail profile. For the measured signals, a low-pass filter is used to find an approximation of the same response. In the present study, Eq. (1) is therefore changed into Eq. (2) where $h(F_{lp})$ is a low-pass filter operator (brick frequency domain filter) with low-pass filtering frequency F_{lp} (symbol $*$ is the convolution operator).

$$f(\theta) = \frac{1}{N_r} \sum_{m=1}^{N_r} \sum_{k=1}^{N_l} (\mathbf{d}_{\text{mea}, F_{lp}}^m(k) - \mathbf{d}_{\text{sim}, 60\text{E}}(k))^2, \quad \mathbf{d}_{\text{mea}, F_{lp}} = h(F_{lp}) * \mathbf{d}_{\text{mea}} \quad (2)$$

To determine the appropriate low-pass filtering frequency and demonstrate that the dynamic excitation from the irregularity at the crossing does not significantly influence the calibration results, a simulation-based study was performed as follows. The dynamic vehicle-S&C interaction was simulated for a grid of simulations where each of the six ballast stiffness configurations p in Fig. 8 was simulated for all six crossing geometries c in Fig. 5 and a constant 60E1 rail profile. The beam properties for the crossing rail were the same in all simulations. The study was performed for both soft and stiff rail fastenings in all crossing panels.

The objective function $f(F_{lp})$ in Eq. (3) is formed to compare the low-pass filtered sleeper displacement data with the simulated response for the constant rail profile.

$$f(F_{lp}) = \sum_{p=1}^6 \sum_{c=1}^6 \sum_{k=1}^N (\mathbf{d}_{\text{sim}, F_{lp}}^{p,c}(k) - \mathbf{d}_{\text{sim}, 60\text{E}}^p(k))^2 \quad (3)$$

By minimizing $f(F_{lp})$ with a gradient-based optimization algorithm, the optimum low-pass frequency F_{lp} that removes the transient dynamics from the signal while still preserving the quasi-static track deflection under a presumed constant load for each ballast stiffness configuration was found. The results when using the optimized low-pass frequency for the soft rail fastening are shown in Fig. 9. The results for the stiff rail fastenings are very similar.

As the low-pass filtered curves are in close agreement with the constant rail profile reference for a wide range of crossing geometries, the presented results show a strong decoupling of crossing geometry and track ballast parameters. The optimized low-pass frequency for both pad types is essentially the same (less than 1 % difference) and corresponds to a deformation wavelength of 2.3 m, or 19.3 Hz at a train speed of 160 km/h.

4. Green's functions - inverse and forward problem formulations

For the inverse load identification and estimation of the crossing rail irregularity, the Green's Kernel Function Method (GKFM) [16-20] is used in this paper to relate the acting wheel-rail contact forces and resulting track (sensor and crossing rail) displacements. In the GKFM, the response of a structure is computed as a convolution integral of the acting load and the unit impulse response function (Green's kernel function) of the structure. The utilized Green's functions are set in the displacement domain as the analysis targets responses at lower frequencies and the physical low-pass filtering of displacements.

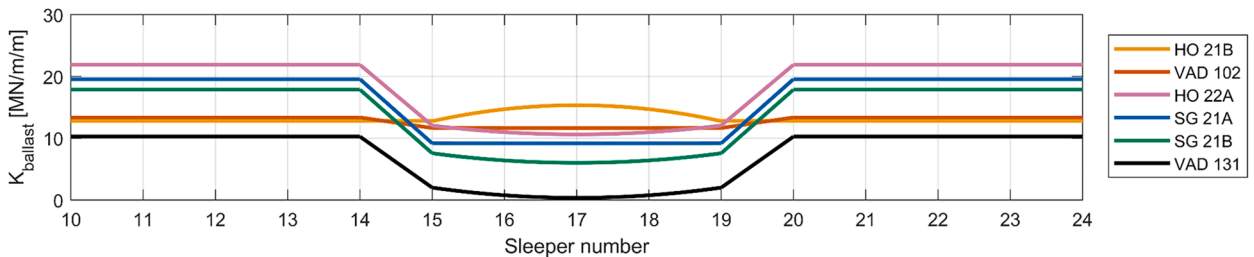


Fig. 8. Calibrated track ballast stiffnesses for six instrumented and scanned S&C. The sensor is located at sleeper 17.

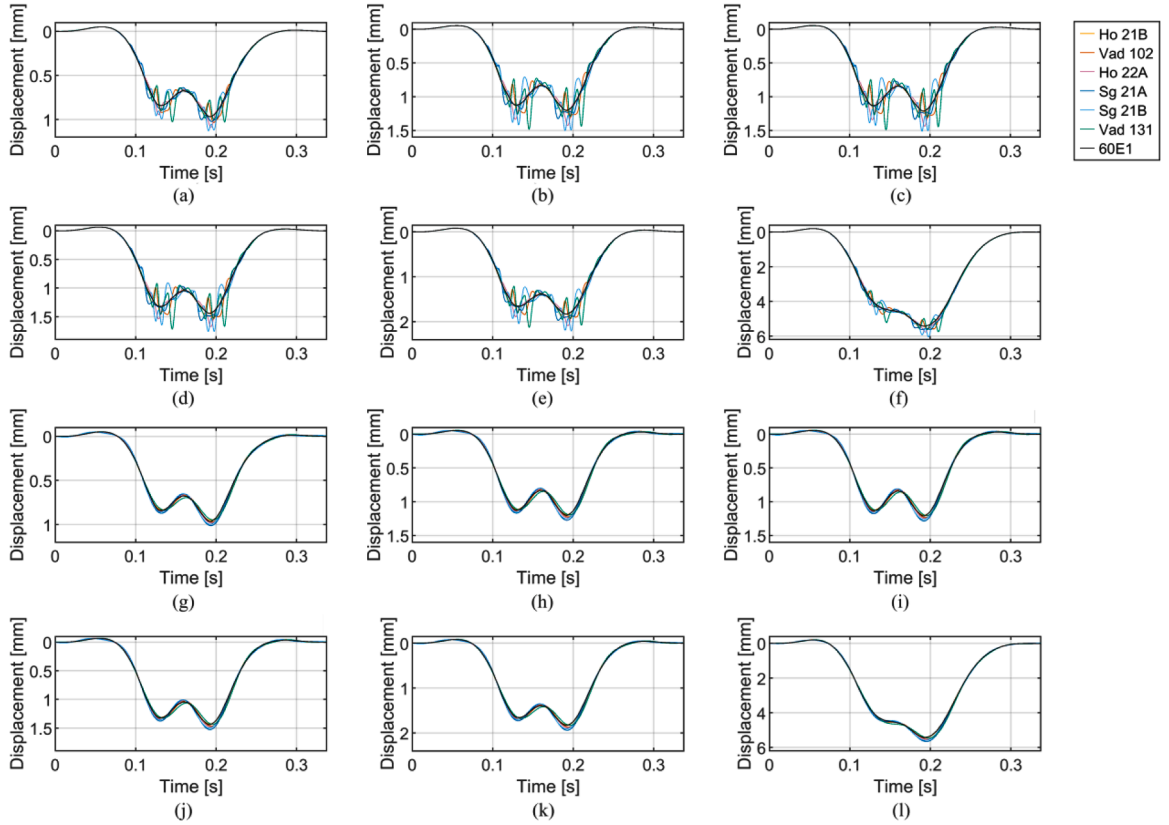


Fig. 9. Simulated sleeper displacement data for the six scanned crossing geometries in Fig. 5 and nominal 60E1 rail profile for the six ballast stiffness distributions in Fig. 8. Unfiltered data is presented in the first two rows of subfigures (a-f, Ho 21B-Vad 131 ballast properties), while the last two rows show data filtered with the optimized low-pass frequency (g-l, Ho 21B-Vad 131 ballast properties). The results were generated for soft rail fastenings in the track model.

4.1. Green's kernel function method for fixed response (GKFM-FR)

In this section, the GKFM is presented. It establishes a relation between the moving vertical wheel–rail contact force and the system response at a fixed sensor location. First, the Green's function for the relationship between the force applied at a fixed point and the response at a fixed point is presented. Then, based on these Green's functions and discretization in the temporal and spatial domains, the relationship between the moving force and response at a fixed point is obtained in a time-discretized matrix formulation.

The unit impulse response function $g_s^{r_m}(t)$ (Green's function) for the time-domain relationship between one force acting at the fixed node location r_m (rail node m) and the response at the fixed sensor location S is calculated using the inverse Fourier transform of the track receptance $h_s^{r_m}(\omega)$. The track receptance in the frequency domain for the corresponding nodal locations is computed from the

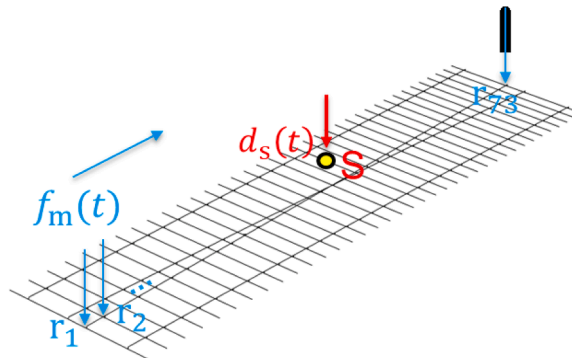


Fig. 10. Single Green's function spatial input-output relation and used track structure model.

calibrated FEM model [47]. The equation is given in Eq. (4) (with \mathcal{F}^{-1} being the inverse Fourier transform operator):

$$g_S^r(t) = \mathcal{F}^{-1} h_S^r(\omega) \quad (4)$$

By considering several fixed positions of the force acting along the crossing panel, the track structure and the force and sensor nodes are illustrated in Fig. 10. The FEM model is meshed such that it has 73 nodes along the straight route rails.

In Fig. 11, the 73 Green's functions relating the force at 73 rail nodes and the response at the sensor node are presented. As expected, it can be observed that the nodes near the sensor have a much greater influence on the sensor response, while excitation at nodes further away has a smaller influence. For example, when the force is acting at three sleeper bays away from the sensor, the maximum of the impulse response function is only about 20 % of the maximum for an excitation directly above the sensor. For the relatively low frequencies of sleeper vibration, condition monitoring with a fixed sensor in track can therefore be described as “nearsighted” due to the high attenuation of the impulse along the track.

For a single force f_{r_m} acting at rail node m (r_m), the displacement response d_S^m at the sensor S can be computed with a convolution integral as shown in Eq. (5) ([28], the symbol $*$ being the convolution operator):

$$d_S^m(t) = \int_0^t g_S^m(\tau) f_{r_m}(t - \tau) d\tau = g_S^m(t) * f_{r_m}(t) \quad (5)$$

The discretized version of $d_S^m(t)$, $g_S^m(t)$ and $f_{r_m}(t)$ are denoted as $d_S^m(n)$, $g_S^m(n)$ and $f_{r_m}(n)$, respectively, while the corresponding time steps for a uniformly discretized time duration with N steps are obtained as $t = \Delta t(n - 1)$. The convolution operation of Eq. (5) can be written in matrix format as shown in Eq. (6) [16]:

$$\begin{bmatrix} d_S^{r_m}(n_1) \\ d_S^{r_m}(n_2) \\ \vdots \\ d_S^{r_m}(n_N) \end{bmatrix} = \begin{bmatrix} g_S^{r_m}(n_1) & 0 & \dots & 0 \\ g_S^{r_m}(n_2) & g_S^{r_m}(n_1) & \dots & 0 \\ \vdots & \vdots & \ddots & \vdots \\ g_S^{r_m}(n_N) & g_S^{r_m}(n_{N-1}) & \dots & g_S^{r_m}(n_1) \end{bmatrix} \begin{bmatrix} f_{r_m}(n_1) \\ f_{r_m}(n_2) \\ \vdots \\ f_{r_m}(n_N) \end{bmatrix} \Delta t \quad (6)$$

or in compact form as (with $G_S^{r_m}$ being the Green's kernel matrix constructed from Green's functions $g_S^{r_m}$):

$$d_S^{r_m} = G_S^{r_m} f_{r_m} \Delta t$$

In order to derive the Green's kernel matrix for a moving load, a superposition of Eq. (6) is made by summing the contributions to the displacement response d_S from forces acting at all nodes r_m as in

$$d_S = \sum_{m=1}^N G_S^{r_m} f_{r_m} \Delta t \quad (7)$$

Further, a force-discretization is introduced, where f_{r_m} is only non-zero at node m at timestep m (when the force is positioned at node m). Thus, the load acts only once at each node and moves at speed $= \frac{\Delta l}{\Delta t}$ where Δl is the distance between each equidistant node. This means that only column m of $G_S^{r_m}$ (every element of column m) is multiplied by a single $f_{r_m}(n_m)$ value. Thus, each summation term in Eq. (7) refers to a single column of $G_S^{r_m}$ and can be written in matrix format as given in Eq. (8):

$$\begin{bmatrix} d_S^{r,v}(n_1) \\ d_S^{r,v}(n_2) \\ \vdots \\ d_S^{r,v}(n_N) \end{bmatrix} = \begin{bmatrix} g_S^{r_1}(n_1) & 0 & \dots & 0 \\ g_S^{r_1}(n_2) & g_S^{r_2}(n_1) & \dots & 0 \\ \vdots & \vdots & \ddots & \vdots \\ g_S^{r_1}(n_N) & g_S^{r_2}(n_{N-1}) & \dots & g_S^{r_N}(n_1) \end{bmatrix} \begin{bmatrix} f_{r_1}(n_1) \\ f_{r_2}(n_2) \\ \vdots \\ f_{r_N}(n_N) \end{bmatrix} \Delta t \quad \text{where } \Delta t = \frac{\Delta l}{v} \quad (8)$$

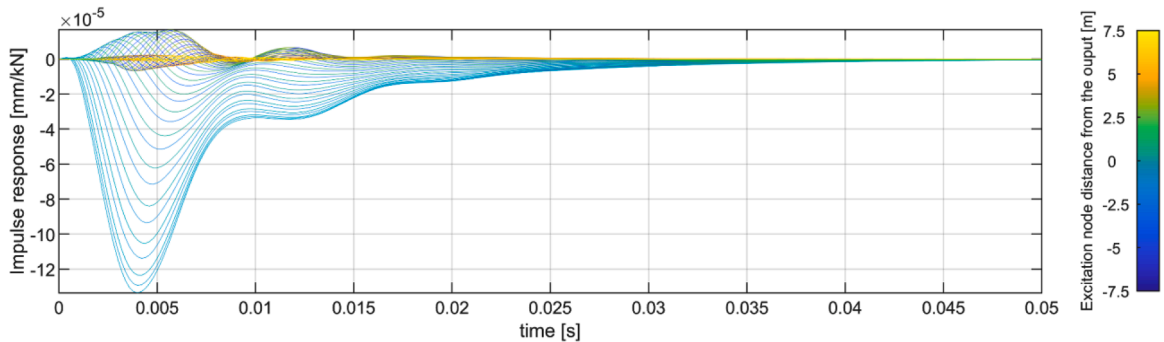


Fig. 11. Example illustrating 73 Green's functions computed for the response at crossing sleeper node S due to impulse force acting at 73 FE rail nodes along a 15 m long track section (corresponding to 15 m bogie travel in the analysis).

For an input force moving along the rail at speed v , the matrix in Eq. (8) is the GKFM for a fixed response $\mathbf{G}_S^{r,v}$ (GKFM-FR) at node S . This equation presents the basis for further inverse problem-solving and moving force identification.

As the FE model is meshed to have 73 nodes along the rail (equidistant spacing 30 cm) on which the force moves, the computed single Green's functions from Fig. 11 need to be spatially interpolated to obtain the needed resolution to fit a particular moving force speed. This resolution also depends on the time-domain sampling rate of the Green's functions. In the performed analysis, the sampling rate of 5000 Hz ($\Delta t = \frac{1}{5000}$ s) is used, which for a moving force at speed $v = 180$ km/h gives the needed spatial resolution $\Delta l = 1$ cm.

In Fig. 12, the interpolated Green's functions for the six calibrated FE models are presented. A correlation between the distribution of ballast stiffness (see Fig. 8) and the magnitudes of the Green's functions is observed. Crossing Ho 21B has the highest ballast stiffness, while Vad 131 has the lowest. Thus, Ho 21B shows the lowest impulse response and Vad 131 the highest. The presented Green's functions have been interpolated to fit particular train speeds to match the field measurements. The train speeds are 180 km/h for Ho 21B, 190 km/h for Ho 22A, 170 km/h for Sg 21A, 160 km/h for Sg 21B, 200 km/h for Vad 102, and 130 km/h for Vad 131. In particular, the Green's functions for Vad 131 can be seen to be distinguished from the rest because of the lower train speed. Further, as the Ho 21B and Ho 22A are 60E crossing panels with softer rail fastenings, their Green's functions show a smoother shape compared to the rest of the crossings.

A convergence study has been performed for the spatial discretization. For the given problem, it was concluded that the chosen mesh size (equidistant node spacing on the rails = 0.3 m) in the track model is optimal such that the applied interpolation method for changing the spatial resolution of the Green's functions provides acceptable accuracy compared to the much more computationally demanding method of explicitly computing the Green's functions for each discretization step.

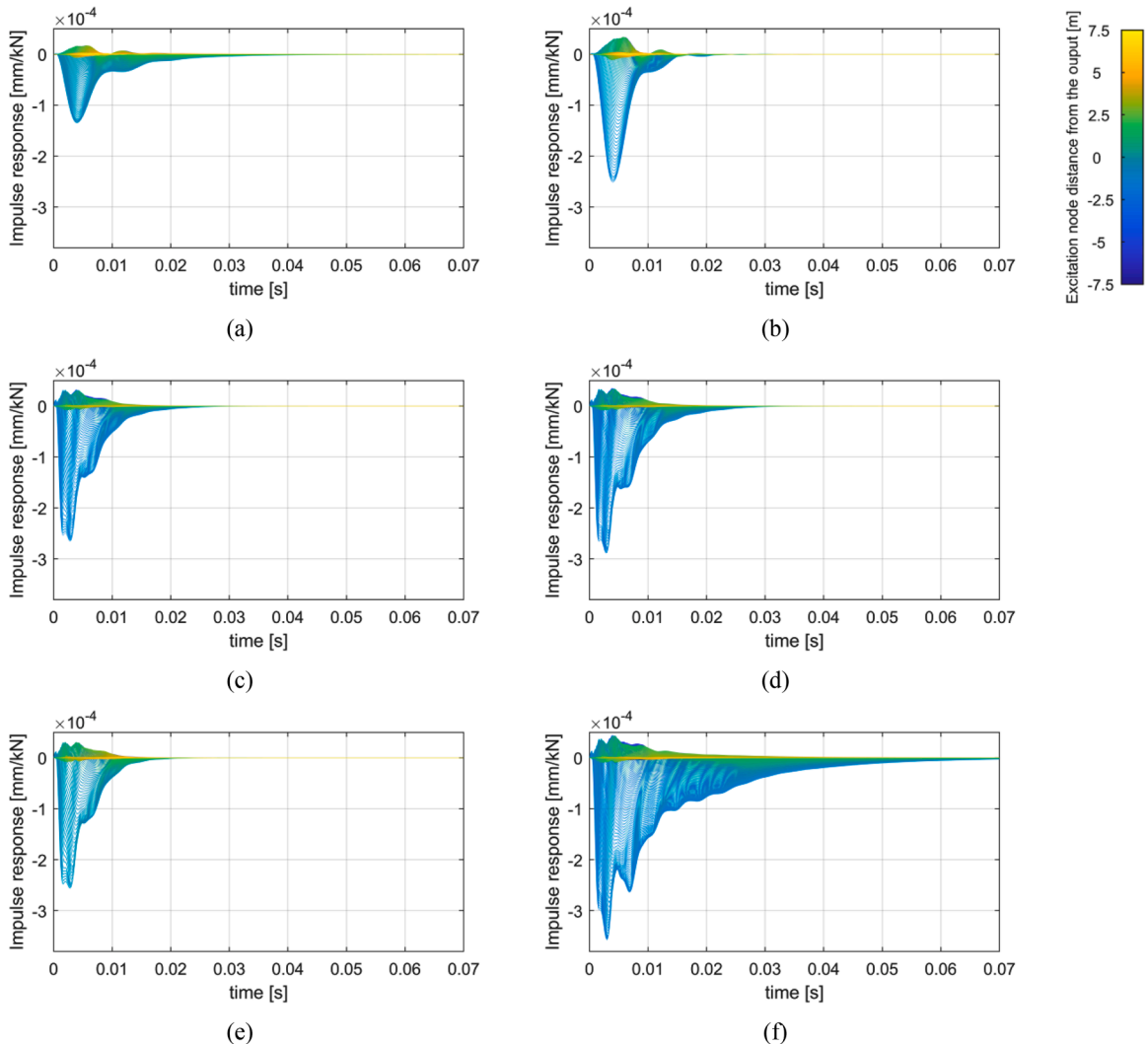


Fig. 12. Interpolated Green's functions. Crossing panel Ho 21B (a), Ho 22A (b), Sg 21A (c), Sg 21B (d), Vad 102 (e) and Vad 131 (f).

4.2. Inverse problem – identification of wheel–rail contact forces

While the relation between a moving load and the sensor has been established in (Eq. (8)), a passing train has more than one wheel that influences the sleeper response. In this paper, the inverse problem is therefore formulated for a four-wheel single-bogie passage as it is assumed that axles further away will have a minor influence on the response based on the “nearsightedness” of the sensor as discussed above. Thus, the GKFM-FRs that relate four moving wheel–rail contact forces $\mathbf{f}_{r,v}$ along two rails (see Fig. 13 for force labels) with the displacement response $d_s^{r,v}$ at sleeper node S (see Eq. (9)) becomes a superposition of the contributions from all four wheels:

$$\mathbf{d}_s^{\text{bogie},v}(n) = \mathbf{G}_s^{\text{fr},v} \mathbf{f}_{\text{fr},v}(n) + \mathbf{G}_s^{\text{fl},v} \mathbf{f}_{\text{fl},v}(n) + \mathbf{G}_s^{\text{rr},v} \mathbf{f}_{\text{rr},v}(n) + \mathbf{G}_s^{\text{rl},v} \mathbf{f}_{\text{rl},v}(n) \quad (9)$$

Further, the idea is to formulate the inverse problem related only to the isolated sleeper displacement response $\mathbf{d}_s^{\text{bogie},v}$ in the sequence interval $n_{\text{tr}1}$ to $n_{\text{tr}2}$, which is the displacement response for the time interval when the front right wheel is passing through the marked transition region TR in Fig. 13, see Eq. (10). The following equations Eq. (10) to Eq. (12) use a notation for a subvector or submatrix of a vector and a matrix as a subscript of the squared bracket related to the vector or matrix ($[\mathbf{v}]_{n_1:n_2}$, $[\mathbf{M}]_{n_1:n_2,n_1:n_2}$). Generally, as the scalar product of one row in the GKFM and one column in the force vector sums up to one sequence of $\mathbf{d}_s^{\text{bogie},v}$, the rows of GKFM are truncated while the force vectors are unaltered. This implies that a force positioned outside of the transition region influences the response $[\mathbf{d}_s^{\text{bogie},v}]_{n_{\text{tr}1}:n_{\text{tr}2}}$ as

$$[\mathbf{d}_s^{\text{bogie},v}]_{n_{\text{tr}1}:n_{\text{tr}2}} = [\mathbf{G}_s^{\text{fr},v}]_{n_{\text{tr}1}:n_{\text{tr}2},1:N} [\mathbf{f}_{\text{fr},v}]_{1:N} + [\mathbf{G}_s^{\text{fl},v}]_{n_{\text{tr}1}:n_{\text{tr}2},1:N} [\mathbf{f}_{\text{fl},v}]_{1:N} + [\mathbf{G}_s^{\text{rr},v}]_{n_{\text{tr}1}:n_{\text{tr}2},1:N} [\mathbf{f}_{\text{rr},v}]_{1:N} + [\mathbf{G}_s^{\text{rl},v}]_{n_{\text{tr}1}:n_{\text{tr}2},1:N} [\mathbf{f}_{\text{rl},v}]_{1:N} \quad (10)$$

Next, by trivial separation of parts of the right front wheel and right rear wheel forces, the domain $n_{\text{tr}1}$ to $n_{\text{tr}2}$ is isolated, see Eq. (11). This formulation takes into account an assumption that the rear wheel force is equal to the front wheel force shifted in time corresponding to the length of the bogie axle spacing n_{bogie} ($\mathbf{f}_{\text{rr},v}(n) = \mathbf{f}_{\text{fr},v}(n + n_{\text{bogie}})$), thus enabling the front wheel force expression $[\mathbf{f}_{\text{fr},v}]_{n_{\text{tr}1}:n_{\text{tr}2}}$ to represent both forces acting in the crossing.

$$[\mathbf{f}_{\text{fr},v}]_n = \begin{bmatrix} [\mathbf{f}_{\text{fr},v}]_{1:n_{\text{tr}1}} \\ [\mathbf{f}_{\text{fr},v}]_{n_{\text{tr}1}:n_{\text{tr}2}} \\ [\mathbf{f}_{\text{fr},v}]_{n_{\text{tr}2}:N} \end{bmatrix}, \quad [\mathbf{f}_{\text{rr},v}]_n = \begin{bmatrix} [\mathbf{f}_{\text{rr},v}]_{1:n_{\text{tr}1}+n_{\text{bogie}}} \\ [\mathbf{f}_{\text{rr},v}]_{n_{\text{tr}1}:n_{\text{tr}2}} \\ [\mathbf{f}_{\text{rr},v}]_{n_{\text{tr}2}+n_{\text{bogie}}:N} \end{bmatrix} \quad (11)$$

By combining the expressions for the isolated sequence interval $n_{\text{tr}1}$ to $n_{\text{tr}2}$ from Eq. (10), and decomposing the forces as in Eq. (11), the inverse problem for identifying the contact force in the transition region, $[\mathbf{f}_{\text{fr},v}]_{n_{\text{tr}1}:n_{\text{tr}2}}$ is derived and presented in Eq. (12).

Further, an additional prerequisite for solving Eq. (12) is that forces outside of the transition region are assumed to be known and equal to the quasi-static force due to the axle load of the identified train type. This means that all forces from the right-hand side of Eq. (12) are assumed to be known and equal to half of the axle load.

The formed matrix ($\mathbf{G}_s^{\text{fr},v} + \mathbf{G}_s^{\text{rr},v}$) is an ill-conditioned, square matrix. Here, the inversion of this matrix is carried out by a Moore–Penrose left pseudo-inverse operation (\dagger) [48,49], which is based on singular value decomposition. For numerical computation, the tolerances related to the singular values of this pseudo-inversion operation are optimized by minimizing the difference between the (1) input displacements and the (2) displacements computed with the Green’s functions and inversely identified forces. The method shows high stability and robustness for the displacement frequency spectrum up to 250 Hz, where most of the displacement energy is. For a higher frequency spectrum with very low displacement energy, diverging results have been observed.

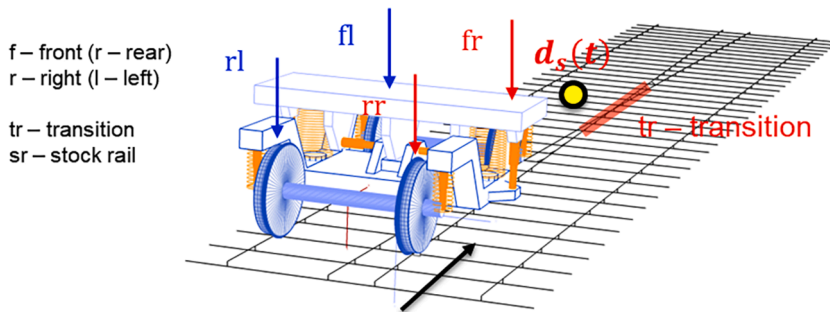


Fig. 13. Bogie vehicle and track models with nomenclature for wheels, and sensor location marked with yellow dot. Marked transparent red region shows the section in which the wheel–rail contact forces are identified. (For interpretation of the references to colour in this figure legend, the reader is referred to the web version of this article.)

$$\begin{aligned}
\left[\mathbf{f}_{fr,v} \right]_{n_{tr1}:n_{tr2}} &= \left(\left[\mathbf{G}_S^{fr,v} \right]_{n_{tr1}:n_{tr2},n_{tr1}:n_{tr2}} + \left[\mathbf{G}_S^{rr,v} \right]_{n_{tr1}:n_{tr2},n_{tr1}+n_{bogie}:n_{tr2}+n_{bogie}} \right)^\dagger \cdot \left(\left[\mathbf{d}_S^{fr, fl, rr, rl, v} \right]_{n_{tr1}:n_{tr2}} - \left[\mathbf{G}_S^{fl,v} \right]_{n_{tr1}:n_{tr2},1:N} \left[\mathbf{f}_{fl,v} \right]_{1:N} \right. \\
&\quad - \left[\mathbf{G}_S^{rl,v} \right]_{n_{tr1}:n_{tr2},1:N} \left[\mathbf{f}_{rl,v} \right]_{1:N} - \left[\mathbf{G}_S^{fr,v} \right]_{n_{tr1}:n_{tr2},1:n_{tr1}} \left[\mathbf{f}_{fr,v} \right]_{1:n_{tr1}} - \left[\mathbf{G}_S^{fr,v} \right]_{n_{tr1}:n_{tr2},n_{tr2}:N} \left[\mathbf{f}_{fr,v} \right]_{n_{tr2}:N} \\
&\quad \left. - \left[\mathbf{G}_S^{rr,v} \right]_{n_{tr1}:n_{tr2},1:n_{tr1}+n_{bogie}} \left[\mathbf{f}_{rr,v} \right]_{1:n_{tr1}+n_{bogie}} - \left[\mathbf{G}_S^{rr,v} \right]_{n_{tr1}:n_{tr2},n_{tr2}+n_{bogie}:N} \left[\mathbf{f}_{rr,v} \right]_{n_{tr2}+n_{bogie}:N} \right)
\end{aligned} \quad (12)$$

In conclusion, the inverse problem formulation for the wheel–rail contact force identification at the transition relies on three assumptions: (I) the time histories of the front and rear wheel–rail contact forces on the crossing rail side are the same but just shifted in time (the time shift corresponding to bogie axle distance); (II) the front and rear wheel–rail contact forces on the stock rail side are constant and equal to half of the known quasi-static axle load; and (III) the front and rear wheel–rail contact forces on the crossing rail side outside of the transition region are constant and equal to half of the known quasi-static axle load, see Fig. 13 for the illustration of the crossing transition. This formulation of the inverse problem transforms the ill-posed problem of identifying four unknown wheel–rail contact forces from one output response to a problem of identifying one force from one output response, thus enabling stable inverse problem-solving with a unique solution.

4.3. Green's functions kernel matrix for moving response (GKFM-MR)

In this section, the Green's function method is instead formulated for the relation between the response of a moving point due to a moving force using GKFM-MR. It is given in Eq. (13), and derived analogously to Eq. (8) via a superposition of impulse response contributions \mathbf{g}_{rj}^i between rail excitation node i and rail response node j . Thus, this formulation requires the impulse response functions to be computed between each rail excitation node to all rail nodes downstream from it where the rail response is to be obtained.

$$\begin{bmatrix} \mathbf{d}_{r1}^{r,v}(n_1) \\ \mathbf{d}_{r2}^{r,v}(n_2) \\ \vdots \\ \mathbf{d}_{rN}^{r,v}(n_N) \end{bmatrix} = \begin{bmatrix} \mathbf{g}_{r1}^{r1}(n_1) & 0 & \dots & 0 \\ \mathbf{g}_{r2}^{r1}(n_2) & \mathbf{g}_{r2}^{r2}(n_1) & \dots & 0 \\ \vdots & \vdots & \ddots & \vdots \\ \mathbf{g}_{rN}^{r1}(n_N) & \mathbf{g}_{rN}^{r2}(n_{N-1}) & \dots & \mathbf{g}_{rN}^{rN}(n_1) \end{bmatrix} \begin{bmatrix} \mathbf{f}_{r1}(n_1) \\ \mathbf{f}_{r2}(n_2) \\ \vdots \\ \mathbf{f}_{rN}(n_N) \end{bmatrix} \Delta t \quad (13)$$

The full expression for the moving rail displacement under the front right wheel–rail contact excited by the four wheel–rail contact forces of one bogie is presented in Eq. (14):

$$\mathbf{d}_{fr,v}^{bogie,v}(n) = \mathbf{G}_{fr,w}^{fr,v} \mathbf{f}_{fr,v}(n) + \mathbf{G}_{fr,w}^{fl,v} \mathbf{f}_{fl,v}(n) + \mathbf{G}_{fr,w}^{rr,v} \mathbf{f}_{rr,v}(n) + \mathbf{G}_{fr,w}^{rl,v} \mathbf{f}_{rl,v}(n) \quad (14)$$

To calculate the rail displacements $\mathbf{d}_{fr,v}^{bogie,v}$, the identified wheel–rail contact forces from the inverse problem-solving are used. These rail displacements together with the wheel displacements will be used to reconstruct the relative wheel–rail trajectories that will be presented in the next section.

5. Crossing irregularity reconstruction

In this section, the formulation of the crossing irregularity reconstruction problem is presented. For a perfectly round wheel making the crossing transition, the irregularity represents the vertical profile of the wheel movement with respect to the rail.

The steps for determining the irregularity are as follows:

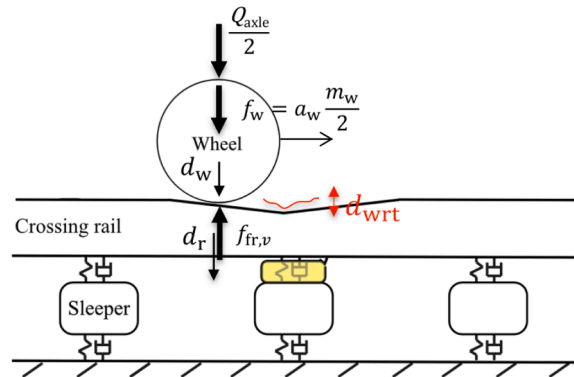


Fig. 14. Free body diagram between the (1) half axle load, (2) mass and acceleration of the wheelset, and (3) inversely identified wheel–rail contact force.

1. Formulation of a Free Body Diagram (FBD) for the wheel, where the wheel load $Q_{axle}/2$ and the inversely identified wheel–rail contact force $f_{fr,v}$ (front right wheel) are acting, see Fig. 14. The wheel load is assumed to be constant and independent of the wheel displacement. This is reasonable since the relatively small wheel displacements would only result in minor changes in the spring suspension forces.
2. Calculation of the wheel acceleration based on the formulated FBD, see Eq. (15). Thus,

$$a_w(t) = \frac{\frac{Q_{axle}(t)}{2} - f_{fr,v}(t)}{\frac{m_w}{2}} \quad (15)$$

3. Integration of the absolute wheel displacement from the calculated wheel acceleration.
4. Calculation of rail displacement beneath the wheel contact point using the identified wheel–rail contact forces and GKFM-MR, see Eq. (14).
5. Calculation of the relative difference between the displacement of the wheel and the rail. This is the crossing irregularity, see Eq. (16).

The wheel displacement calculation in step 3 is a double integration performed in the frequency domain analogous to the method presented in [13]. The result from step 5 is the wheel–rail relative vertical displacement that is governed by the discontinuity of the crossing in the transition from wing rail to crossing nose. The equation for calculation of the irregularity is presented in Eq. (16):

$$d_{wrt}(t) = \int_0^t \int_0^{\tau'} a_w(\tau) d\tau d\tau' - d_{fr}^{bogie,v}(t) \quad (16)$$

Further, the computed d_{wrt} is band-pass filtered into the results $d_{wrt, bp}$ such that it disregards irregularity wavelengths longer than 1 m, as the shorter geometric characteristics are of greater interest and contribute more to the dynamic contact forces generated in the crossing panel. Also, difficulties would arise in the low-frequency region in terms of the integration of wheel displacement from accelerations. This is due to the short duration of the acceleration signal that concerns the wheel passing through a transition region of 2.4 m, which for a train speed of 180 km/h (50 m/s) is approximately 0.05 s corresponding to 20 Hz. Consequently, the 2.4 m is the ultimate lower limit for the bandpass filter, while the upper limit is 250 Hz stemming from the limit used to filter the identified forces. In the results presented in the next section, the maximum wavelength has been set to 1 m (< 2.4 m). Depending on train speed, the

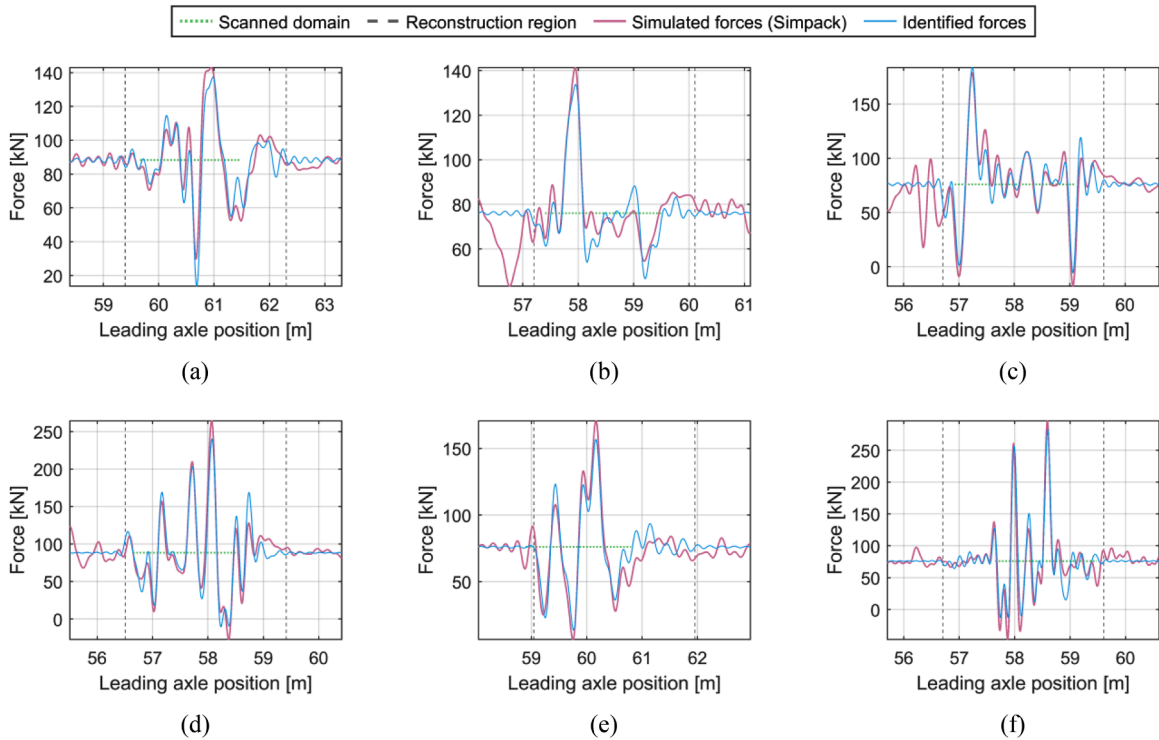


Fig. 15. Simulated and identified wheel–rail contact forces, low-pass filtered at 250 Hz: crossing panel Ho 21B (a), Ho 22A (b), Sg 21A (c), Sg 21B (d), Vad 102 (e), Vad 131 (f).

minimum wavelength is determined by the upper-frequency limit of 250 Hz.

6. Results and validation

In this section, a verification and validation of the presented method is presented. The section is separated into two subsections concerning (I) results obtained with simulation data, and (II) results obtained with measured field data. Thus, the verification of the method concerns both (I) an analysis with simulation data that has ground truth, and (II) analyses with measured field data from multiple crossings and comparisons to the true field crossing rail scans. Again, the overall workflow for reconstructing crossing rail geometry from measured accelerations is illustrated in Fig. 2.

6.1. Simulation data

This subsection presents analysis performed with simulation data. The workflow concerns (I) inverse force identification from simulated sleeper displacements, and (II) crossing irregularity reconstruction.

6.1.1. Inverse force identification

As described in Section 4.2, the inverse force identification uses measured sleeper displacement as input together with the inverted moving Green's functions kernel matrix. The sleeper displacement responses used for identifying the forces presented in this subsection have been calculated using the calibrated MBS models for the six crossing panels with their actual scanned crossing geometries implemented. The presented results, see Fig. 15, show the comparison between the inversely identified forces and the true forces calculated with the MBS model. The Green's functions from which the GKFM-FR is computed are sampled at 5000 Hz (shown in Fig. 12). In [13], it was shown that sleeper displacement responses have most of the energy in the frequency range up to about 80 Hz. Thus, the 250 Hz limit is here considered as sufficient to capture the displacement energy and to avoid introducing any high-frequency noise.

The applied train speed and axle load for the six crossing panel MBS models are: HO 21B 180 km/h and 18 t; HO 22A 190 km/h and 15.5 t, SG 21A 170 km/h and 15.5 t, SG 21B 160 km/h and 18 t, VAD 102 200 km/h and 15.5 t, VAD 131 130 km/h and 15.5 t. As described in Section 5, the inversely identified forces and the true simulation forces are low-pass filtered at 250 Hz. This limit is due to the low influence of the higher frequency force content on the displacement response.

Overall, the identified wheel–rail contact forces show good agreement with the calculated wheel–rail contact forces from the MBS models both in terms of signature and magnitude, with slightly lower magnitudes for the identified forces. The presented sample of results shows the identified forces for the 2.4 m long transition region and part of the outer region with the quasi-static force. The observed ripples for the quasi-static part of the identified force and the negative values (indicating physical loss of contact) for both the

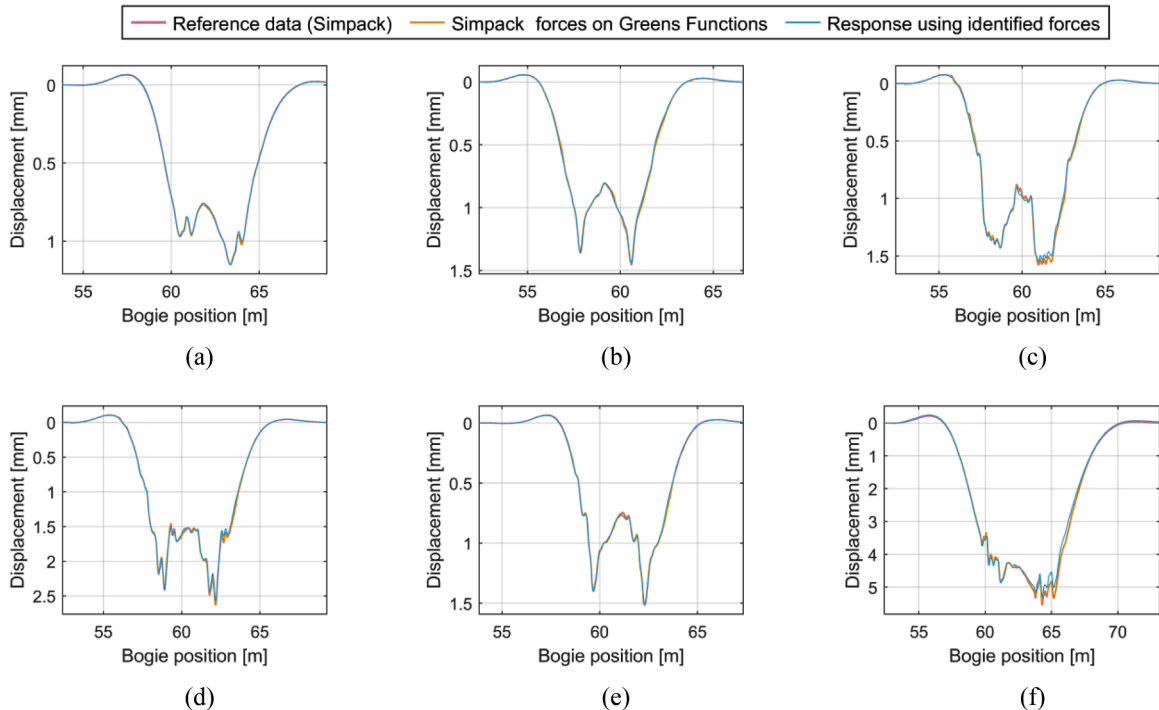


Fig. 16. Simulated sleeper displacements: crossing panel Ho 21B (a), Ho 22A (b), Sg 21A (c), Sg 21B (d), Vad 102 (e), Vad 131 (f).

simulated and identified forces stem from the low-pass filtering.

In Fig. 16, sleeper displacement for three cases are presented: (I) computed with Simpack MBS and used as input for the inverse force identification, (II) computed with Simpack MBS forces and Green's functions, and (III) computed from inversely identified forces and Green's functions. These results constitute a verification of the method in a simulation environment. It is observed that applying the true MBS forces to compute the sensor displacement using the GKFM-FR yields more or less exactly the same results as the true simulated sensor displacements. This means that the Green's functions give a very accurate representation of the dynamic track properties. The discrepancy between the simulated and identified forces therefore stems from the solution of the inverse problem itself and the pseudo-inverse.

6.1.2. Crossing irregularity reconstruction

This section presents the results from the crossing irregularity reconstruction for the six crossing panels, see Fig. 17. The presented results refer to the reconstruction of the band-pass filtered irregularity from the MBS sleeper displacements and a comparison with the actual calculated irregularity from the MBS analysis. The displayed results demonstrate a high level of agreement between the reconstructed irregularity and the actual irregularity, showing that it is possible to reconstruct the rail geometry based on measured sleeper accelerations. Additionally, multiple momentum sign changes are observed indicating that the assumption of a single dip angle [14] does not fully describe the crossing rail geometrical state.

In the context of crossing panel monitoring, this irregularity can serve as an indicator of the rail geometry condition that can be corrected through repairs. The irregularity also reveals the location where the wheel transitions from the wing rail to the crossing nose, possibly highlighting a fatigued area [3].

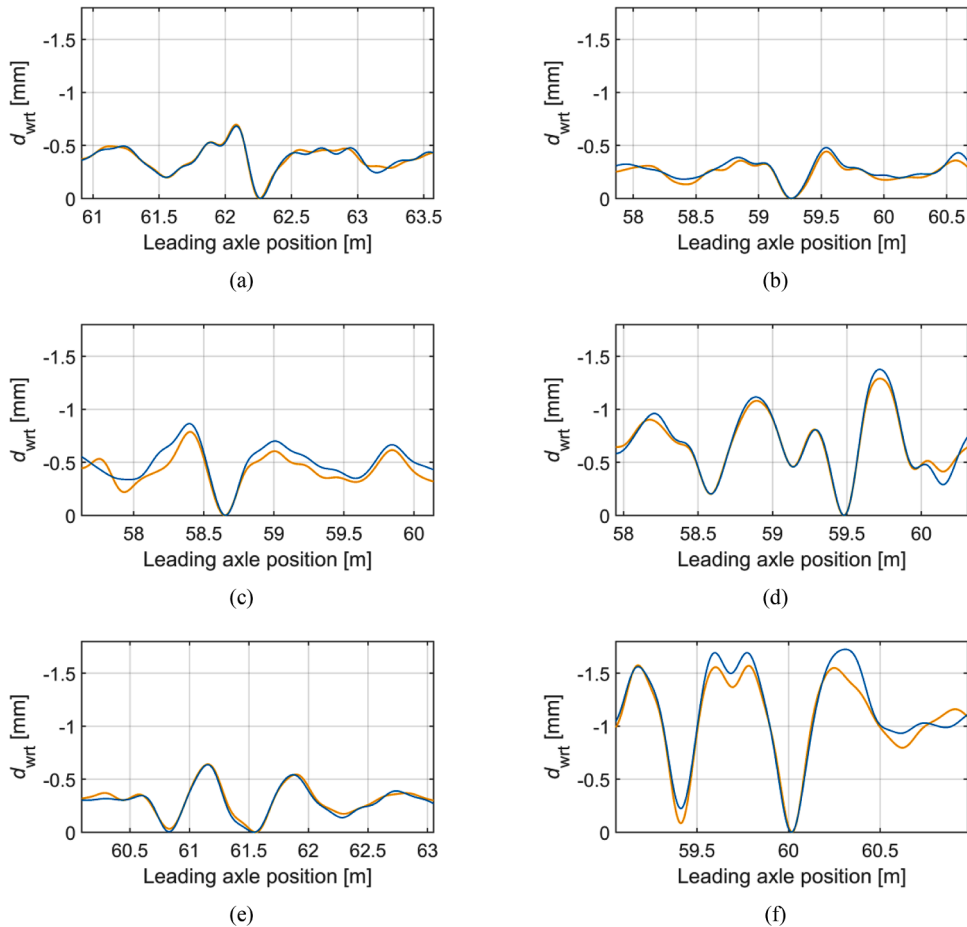


Fig. 17. Band-pass filtered wheel–rail trajectories ($d_{wrt, bp}$, crossing irregularities) from MBS simulations (yellow) and reconstruction method (blue): crossing panel Ho 21B (a), Ho 22A (b), Sg 21A (c), Sg 21B (d), Vad 102 (e), Vad 131 (f). The signals have been shifted to coincide at their peak values. The larger the $d_{wrt, bp}$ value (positive direction), the further the wheel has moved down into the track. (For interpretation of the references to colour in this figure legend, the reader is referred to the web version of this article.)

6.2. Measurement data and simulation data for validation

In this section, results from the identification of force and crossing irregularity are presented for three of the six studied crossing panels and for a sample of train passages. For the purpose of method and results validation, the results are compared with the results from the MBS simulations with the calibrated ballast stiffness and laser-scanned crossing geometries. For each crossing panel using 17 different scanned wheel profiles that cover a wide range of wheel profile shapes [14] are used. While the actual crossing geometries of the studied crossing panels are known, the corresponding wheel profiles in traffic and their path through the crossing panel are not. This motivates the comparison between measurement and simulation on a sample level. The results presented in Fig. 18 to Fig. 20 are: (I) reconstructed sleeper displacements used as input for identifying wheel–rail contact forces, (II) inversely identified wheel–rail contact forces, and (III) reconstructed vertical irregularities along the crossing transition contact path. Each figure shows the (i) dynamic responses from individual bogies passing through the crossing panel, (ii) regions corresponding to the 80th percentile of all corresponding dynamic responses (20 % of results excluded), and (iii) the first mode of the singular value decomposition (SVD) [49] that serves as a representation of the underlying dominant trend in the data. Details concerning S&C type, traffic and scan details, and total train passes are given in Table 2.

The results show that there is a significant repeatability of the reconstructed sleeper displacements, but dispersion for the force and irregularity results. This is expected as the identified forces and trajectories depend on the lateral position of the wheel–rail contact

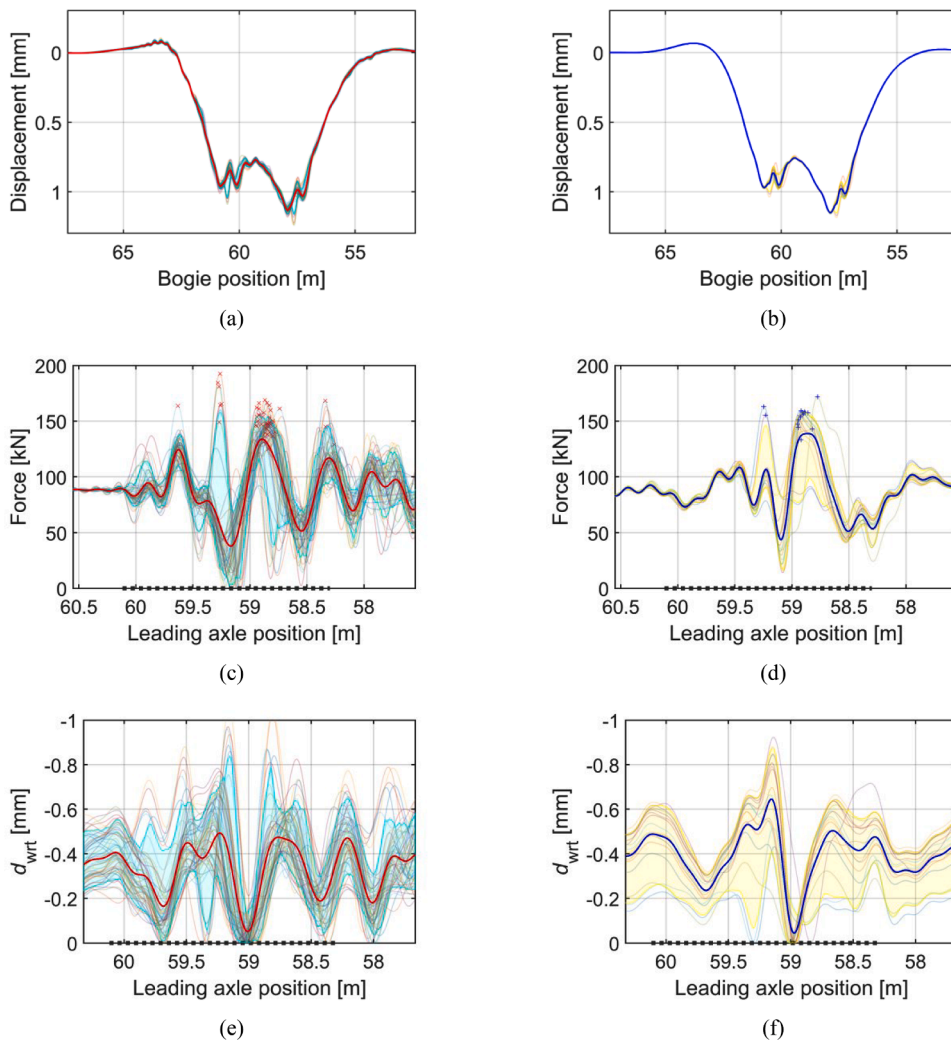


Fig. 18. Results for Crossing panel Ho 21B. Reconstructed field measurements of (a) sleeper displacements, (c) wheel–rail contact forces, and (e) crossing irregularities. Simulation results for (b) sleeper displacements, (d) wheel–rail contact forces, and (f) crossing irregularities. The figures show individual responses for different bogie passes, regions corresponding to the 80th percentile of all results (cyan and yellow transparent fields), and the first mode of SVD decomposition (thick red and blue lines). Scatter points in the force diagrams show the maximum magnitude of the force per bogie passage and dotted lines mark the scanned rail region. (For interpretation of the references to colour in this figure legend, the reader is referred to the web version of this article.)

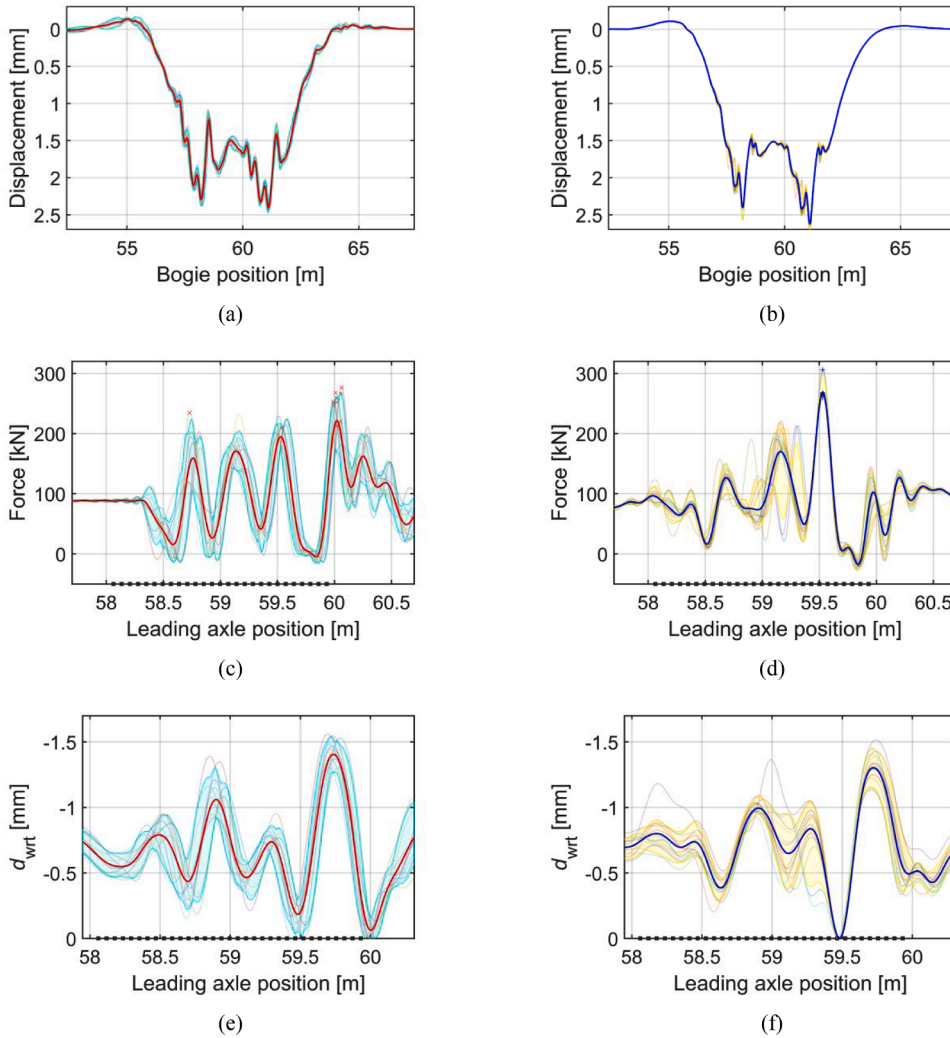


Fig. 19. Crossing panel Sg 21B. See also the caption to Fig. 18.

through the crossing transition, which is influenced by many factors. Firstly, it is influenced by the wheel profile tread angle and concavity caused by wear. It is also influenced by the global wheelset entry position to the crossing panel from the stock rail to the wing or crossing rail, which can shift due to hunting motion. This means that the wheel can negotiate the crossing transition in many ways causing different wheel–rail contact forces and different wheel–rail vertical trajectories. Further, the forces and trajectories may be influenced by various forms of wheel out-of-roundness on different wheels.

The results show that there is a greater variance in responses in the field measurements (except for the two hollow worn wheel profiles that are outliers in the simulations), but a strong qualitative correlation between measurement and simulation. It should also be noted that the crossing scanning lengths are between 1.7 m to 2.5 m, see Fig. 5, while outside of these regions a smooth stock rail profile is assumed. This reduces the length over which the results can be compared, but it also affects the dynamic responses. The scanned rail profiles are processed to be adequately spatially oriented and filtered using a 2D filter and further processed by Simpack with spline functions [14]. All of this leaves a certain margin for error. Regardless, the similarity between reconstructed quantities from measurements and simulations is high.

Overall, a lower match between reconstructed and simulated results is observed for the Vad 131 crossing panel (see Fig. 20). Also for Vad 131 (Fig. 20 top right and mid right), an additional force peak is observed between the two main peaks in the simulation compared to the reconstructed results. This disables the rebound of the system observed in the measurements, thus lowering the depth of the irregularity. Additionally, the third force peak observed in the measurement results (Fig. 20 mid left) is not present in the simulations due to the short scanning region of 1.8 m. Thus, a smooth rail geometry has been assumed in the model for that part of the rail. For Vad 131, it could be the case that a nonlinear model with voided sleepers, and not only a low linear ballast stiffness, would be required as the sleeper displacements are close to 6 mm, which is very large. Nevertheless, the given linear model gives a good estimate of the force magnitude and the shape of the rail irregularity.

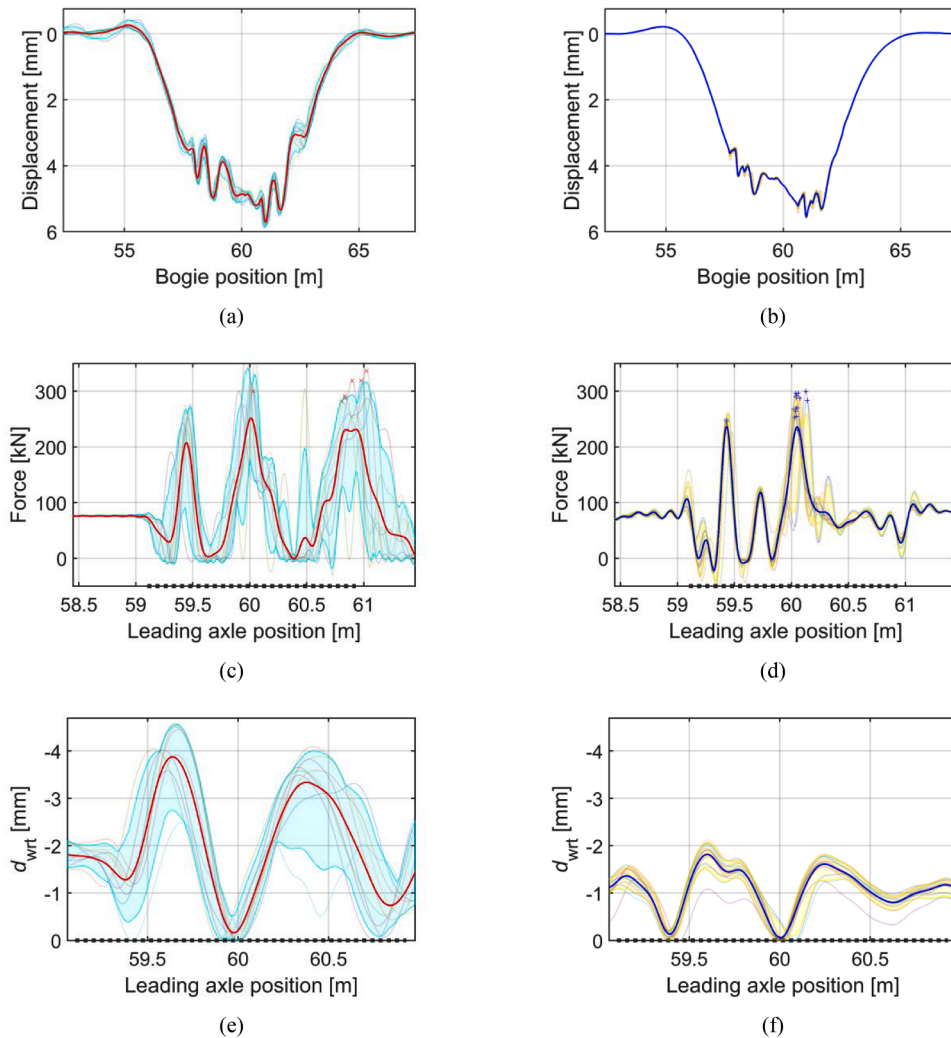


Fig. 20. Crossing panel Vad 131. See also the caption to Fig. 18.

Table 2

Crossing panel and recorded train passage information

Crossing panel	S&C type	Traffic direction	Train speed	Total used train passes*	Scan length
Ho 21B (Fig. 18)	60E	trailing direction	180 km/h	57	1.7 m
Ho 21A	60E	facing direction	190 km/h	48	2.3 m
Sg 21A	UIC60	facing direction	170 km/h	41	2.5 m
Sg 21B (Fig. 19)	UIC60	facing direction	160 km/h	12	1.9 m
Vad 102	UIC60	trailing direction	200 km/h	38	1.6 m
Vad 131 (Fig. 20)	UIC60	facing direction	130 km/h	9	1.8 m

* selection criteria $\pm 5\%$ in train speed range

6.3. Method limitations

The presented Crossing Panel Condition Monitoring (CPCM) method consists of six steps. Each particular step brings certain assumptions and limitations that influence the end result. In the first step, mechanical-vibration-influenced change of electrical current in the sensor is measured and transformed to acceleration. This process is affected by environmental conditions and the temperature of the sensor parts [50], and also the sensor itself can undergo some level of long-term deterioration. Together this negatively contributes to the sensor's digital noise and performance, which makes the remote acceleration data acquisition a sensitive process. An additional difficult challenge related to the temperature effects is to understand and distinguish its influence on the structural response from the sensor performance itself. For example, solar radiation as a source of thermal force can cause a temperature difference between the air

temperature and rail up to 40°C [51]. This can cause an increase in rail stress and possibly rail expansion and track deformation. Conversely, cold weather can induce tension cracks [52]. Thus, the used measurement technology brings an uncertainty limiting the understanding of temperature influence on the end result of the CPCM method. On the other hand, these effects have a larger contribution to the magnitude of the measured responses (scaling effect), thus not jeopardizing the evaluation of the shape of the irregularity which is the overall most important crossing rail condition information.

The second step of the CPCM method reconstructs recorded accelerations into rail displacements using the method developed in [13]. The challenges of the given method are the handling of the low-frequency transients, drift, and signal distortions coming from saturation. The errors coming from the given challenges have a bigger contribution to the low-frequency part of the integrated displacement signal and do not strongly influence the identified force or irregularity because it is high-pass filtered at 1 m wavelength (which corresponds to 50 Hz at train speed 180 km/h or 50 m/s).

In the third and fourth steps covering the ballast stiffness calibration and inverse force identification, linear track properties are assumed. This is partly a prerequisite to be able to use the GKFM approach based on linear theory, but previous work in [15] has also shown that it is not possible to uniquely identify a bi-linear ballast stiffness model based on the track displacement response as different combinations of stiffness and voids can give very similar responses. Linear theory is therefore also considered sufficient to model the present system as demonstrated by the agreement between simulations and measurements.

Finally, in the last step, the crossing irregularity is computed. Here the wheelset mass and therefore the train type needs to be known. This information is mostly only available for passenger trains. Thus, the method is not suitable for freight trains and depends on train classifier algorithm accuracy.

Additionally, for very low speeds (under 40 km/h) impact forces even for large rail irregularities are low. Thus, the method becomes less accurate as the high-pass frequency contents become close to the sensor noise level. This can be addressed with a change of sensor that has lower g measurement limits, but then it becomes not suitable for faster train speeds.

7. Condition indicators

In Fig. 21, the results from all of the studied six crossing panels are summarized to compare the overall agreement between simulated and reconstructed results and to evaluate the accuracy of the derived condition indicators. The condition indicators present a correlation between average simulated and identified maximum force magnitudes, and the RMS of the average irregularity marked in the 80th percentile range for individual wheel passages. A good match is observed for crossings Ho 21B, Ho 22A, Sg 21A and Sg 21B. The differences observed for the Vad crossing panels are expected due to the lower calibration match and possible scanning issues as previously addressed in Section 6.2. Overall, based on both the force and irregularity criteria, the Sg 21B and Vad 131 crossings with the worst crossing irregularities are clearly separated from the others. Compared to the condition indicators from [14], a better match is observed between simulated and measured results. Additionally, a condition threshold separating the healthy and damaged state is estimated. The set threshold is based on identifying the Sg 21B and Vad 131 to be in a damaged condition which can be significantly improved with a maintenance action.

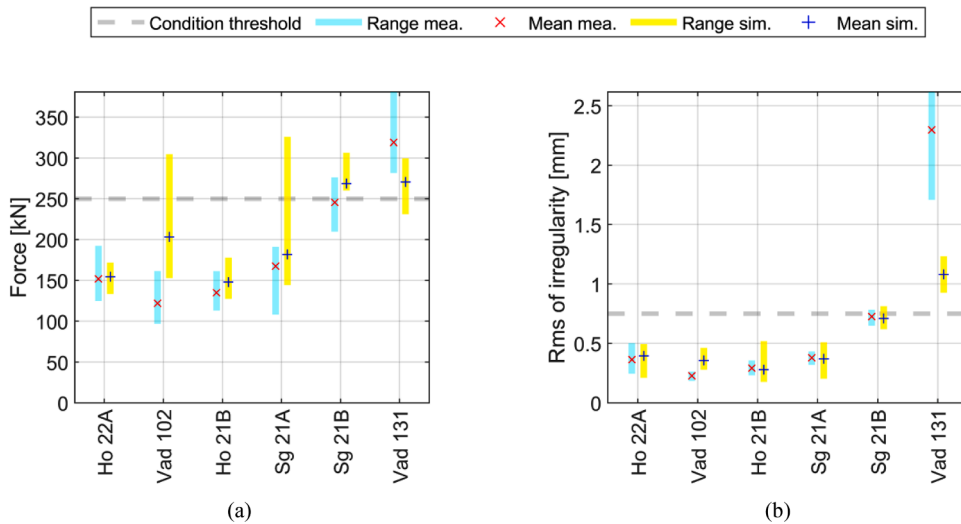


Fig. 21. Condition indicators: force magnitude (a), rms of crossing irregularity (b). Bars are the 80th percentile range of all corresponding dynamic responses, and markers are the mean values.

8. Conclusions

Based on measured sleeper accelerations from embedded sensors and knowledge of the S&C type, this paper has presented a Crossing Panel Condition Monitoring (CPCM) scheme to identify the ballast and crossing geometry conditions. The CPCM has been verified and validated using concurrently measured sleeper accelerations and laser-scanned crossing geometries from six crossing panels in southern Sweden. The scanned crossing geometries have provided a reference that has allowed for validation of the force and irregularity identification schemes.

This paper has shown that it is possible to identify: (I) ballast stiffness properties without knowledge of the actual crossing geometry, (II) wheel–rail contact forces by solving an inverse problem formulated with the use of single-moving GKFM of the calibrated model, and (III) relative wheel–rail trajectories in a band-pass filtered frequency region by using moving GKFM and the identified wheel–rail contact forces. Good agreement was found between quantities identified from measured data and those from a simulation environment. The magnitudes of wheel–rail contact forces and relative wheel–rail trajectories can be directly related to plastic damage and wear evolution rates in a crossing, thus presenting a strong crossing panel condition indicator.

CRedit authorship contribution statement

Marko D.G. Milošević: Writing – review & editing, Writing – original draft, Visualization, Validation, Software, Methodology, Investigation, Formal analysis, Data curation, Conceptualization. **Björn A. Pålsson:** Writing – review & editing, Writing – original draft, Visualization, Validation, Supervision, Resources, Project administration, Methodology, Investigation, Funding acquisition, Formal analysis, Data curation, Conceptualization. **Arne Nissen:** Visualization, Validation, Supervision, Resources, Project administration, Methodology, Investigation, Funding acquisition, Data curation, Conceptualization. **Jens C.O. Nielsen:** Writing – review & editing, Writing – original draft, Visualization, Validation, Supervision, Project administration, Methodology, Investigation, Formal analysis, Conceptualization. **Håkan Johansson:** Writing – review & editing, Writing – original draft, Visualization, Validation, Supervision, Methodology, Investigation, Formal analysis, Conceptualization.

Declaration of competing interest

The authors declare that they have no known competing financial interests or personal relationships that could have appeared to influence the work reported in this paper.

Data availability

The authors do not have permission to share data.

Acknowledgements

The current study is part of the on-going activities in CHARMEC (Chalmers Railway Mechanics, www.chalmers.se/charmec). Parts of the study have been funded within the European Union's Horizon 2020 research and innovation programme in the Shift2Rail projects In2Track2 and In2Track3 under grant agreement nos. 826255 and 101012456. The acceleration data used in this research was acquired with sensors from Konux GmbH and received from Trafikverket (the Swedish Transport Administration).

References

- [1] Increased Capacity4Rail networks through enhanced infrastructure and optimized operations, deliverable D13.1 OPERATIONAL Failure MODEs of S&C, European Commission, Brussels, Belgium, 2015.
- [2] R. Skrypnik, U. Ossberger, B.A. Pålsson, M. Ekh, J.C.O. Nielsen, Long-term rail profile damage in a railway crossing: Field measurements and numerical simulations, *Wear* 472 (2021) 203331, <https://doi.org/10.1016/j.wear.2020.203331>.
- [3] X. Liu, V.L. Markine, H. Wang, I.Y. Shevtsov, Experimental tools for railway crossing condition monitoring (crossing condition monitoring tools), *J. Internat. Measur. Confederat.* 129 (2018) 424–435, <https://doi.org/10.1016/j.measurement.2018.07.062>.
- [4] Y. Bezin, I. Grossoni, S. Neves, Impact of wheel shape on the vertical damage of cast crossing panels in turnouts, in: 24th International symposium on dynamics of vehicles on roads and tracks, Graz, Austria, 2015.
- [5] B.A. Pålsson, A parameterized turnout model for simulation of dynamic vehicle–turnout interaction with an application to crossing geometry assessment, in: The IAVSD international symposium on dynamics of vehicles on roads and tracks, Springer, Gothenburg, Sweden, 2019, pp. 351–358.
- [6] P. Torstensson, G. Squicciarini, M. Krüger, B.A. Pålsson, J.C.O. Nielsen, D.J. Thompson, Wheel–rail impact loads and noise generated at railway crossings—Influence of vehicle speed and crossing dip angle, *J. Sound. Vib.* 456 (2019) 119–136, <https://doi.org/10.1016/j.jsv.2019.04.034>.
- [7] X. Liu, V.L. Markine, Train hunting related fast degradation of a railway crossing - Condition monitoring and numerical verification, *Sensors* 20 (2020) 2278, <https://doi.org/10.3390/s20082278>.
- [8] S. Bruni, I. Anastasopoulos, S. Alfi, A. Van Leuven, G. Gazetas, Effects of train impacts on urban turnouts: modelling and validation through measurements, *J. Sound. Vib.* 324 (2009), <https://doi.org/10.1016/j.jsv.2009.02.016>.
- [9] I. Grossoni, Y. Bezin, S. Neves, Optimisation of support stiffness at railway crossings, *Vehicle Syst. Dyn.* 56 (2018) 1072–1096, <https://doi.org/10.1080/00423114.2017.1404617>.
- [10] M. Pletz, W. Daves, H. Ossberger, A wheel set/crossing model regarding impact, sliding and deformation—Explicit finite element approach, *Wear* 294 (2012) 446–456, <https://doi.org/10.1016/j.wear.2012.07.033>.
- [11] L. Xin, V. Markine, I. Shevtsov, Numerical analysis of the dynamic interaction between wheel set and turnout crossing using the explicit finite element method, *Vehicle Syst. Dyn.* 54 (2016) 301–327, <https://doi.org/10.1080/00423114.2015.1136424>.

- [12] M. Boogaard, Z. Li, R. Dollevoet, In situ measurements of the crossing vibrations of a railway turnout, *Measurement* 125 (2018) 313–324, <https://doi.org/10.1016/j.measurement.2018.04.094>.
- [13] M.D.G. Milošević, B.A. Pålsson, A. Nissen, J.C.O. Nielsen, H. Johansson, Reconstruction of sleeper displacements from measured accelerations for model-based condition monitoring of railway crossing panels, *Mech. Syst. Signal. Process.* 192 (2023), <https://doi.org/10.1016/j.ymssp.2023.110225>.
- [14] M.D.G. Milošević, B.A. Pålsson, A. Nissen, J.C.O. Nielsen, H. Johansson, Condition monitoring of railway crossing geometry via measured and simulated track responses, *Sensors* 22 (2022) 1012, <https://doi.org/10.3390/s22031012>.
- [15] M. Milošević, B. Pålsson, A. Nissen, H. Johansson, J.C.O. Nielsen, Model-based remote health monitoring of ballast conditions in railway crossing panels, in: *Proceedings of the 10th European workshop on structural health monitoring (EWSHM)*, Springer International Publishing, Palermo, Italy, 2022, pp. 502–512.
- [16] J. Liu, X. Sun, X. Han, C. Jiang, D. Yu, A novel computational inverse technique for load identification using the shape function method of moving least square fitting, *Comput. Struct.* 144 (2014) 127–137, <https://doi.org/10.1016/j.compstruc.2014.08.002>.
- [17] L. Zhang, Y. Zhu, H. Zhang, X. Zhu, Identification of dynamic load on cantilever beam using green's function method and regularization technique, in: *39th Chinese Control Conference (CCC)*, IEEE, Shenyang, China, 2020, pp. 2786–2791.
- [18] Y. Sun, L. Luo, K. Chen, X. Qin, Q. Zhang, A time-domain method for load identification using moving weighted least square technique, *Comput. Struct.* 234 (2020) 106254, <https://doi.org/10.1016/j.compstruc.2020.106254>.
- [19] S. Wu, Y. Zheng, Y. Sun, Q. Fei, Identify the stochastic dynamic load on a complex uncertain structural system, *Mech. Syst. Signal. Process.* 147 (2021) 107114, <https://doi.org/10.1016/j.ymssp.2020.107114>.
- [20] S. Wu, Y. Sun, Y. Li, Q. Fei, Stochastic dynamic load identification on an uncertain structure with correlated system parameters, *J. Vib. Acoust.* 141 (2019) 041013, <https://doi.org/10.1115/1.4043412>.
- [21] S. Zhang, G. Cheng, X. Sheng, D.J. Thompson, Dynamic wheel-rail interaction at high speed based on time-domain moving Green's functions, *J. Sound. Vib.* 488 (2020) 115632, <https://doi.org/10.1016/j.jsv.2020.115632>.
- [22] M. Chen, Y. Sun, W. Zhai, High efficient dynamic analysis of vehicle-track-subgrade vertical interaction based on Green function method, *Vehicle Syst. Dyn.* 58 (2020) 1076–1100, <https://doi.org/10.1080/00423114.2019.1607403>.
- [23] S. Qu, J. Yang, Y. Feng, Y. Peng, C. Zhao, S. Zhu, W. Zhai, Ground vibration induced by maglev trains running inside tunnel: Numerical modelling and experimental validation, *Soil Dyn. Earthquake Eng.* 157 (2022) 107278, <https://doi.org/10.1016/j.soildyn.2022.107278>.
- [24] N.C. Dos Santos, J. Barbosa, R. Calçada, R. Delgado, Track-ground vibrations induced by railway traffic: experimental validation of a 3D numerical model, *Soil Dyn. Earthquake Eng.* 97 (2017) 324–344, <https://doi.org/10.1016/j.soildyn.2017.03.004>.
- [25] H. Xia, Y. Cao, G. De Roeck, Theoretical modeling and characteristic analysis of moving-train induced ground vibrations, *J. Sound. Vib.* 329 (2010) 819–832, <https://doi.org/10.1016/j.jsv.2009.10.007>.
- [26] A.M. Kaynia, J. Park, K. Norén-Cosgriff, Effect of track defects on vibration from high speed train, *Procedia Eng.* 199 (2017) 2681–2686, <https://doi.org/10.1016/j.proeng.2017.09.551>.
- [27] X. Sheng, C.J.C. Jones, D.J. Thompson, Responses of infinite periodic structures to moving or stationary harmonic loads, *J. Sound. Vib.* 282 (2005) 125–149, <https://doi.org/10.1016/j.jsv.2004.02.050>.
- [28] A. Pieringer, Time-domain modelling of high-frequency wheel/rail interaction, 2011. Doctoral thesis.
- [29] T.H. Chan, S. Law, T. Yung, X. Yuan, An interpretive method for moving force identification, *J. Sound. Vib.* 219 (1999) 503–524, <https://doi.org/10.1006/jsvi.1998.1904>.
- [30] S.-S. Law, T.H. Chan, Q. Zeng, Moving force identification: a time domain method, *J. Sound. Vib.* 201 (1997) 1–22, <https://doi.org/10.1006/jsvi.1996.0774>.
- [31] Z. Chen, T.H. Chan, A truncated generalized singular value decomposition algorithm for moving force identification with ill-posed problems, *J. Sound. Vib.* 401 (2017) 297–310, <https://doi.org/10.1016/j.jsv.2017.05.004>.
- [32] S. Wu, S. Law, Moving force identification based on stochastic finite element model, *Eng. Struct.* 32 (2010) 1016–1027, <https://doi.org/10.1016/j.engstruct.2009.12.028>.
- [33] S. Pourzeynali, X. Zhu, A. Ghari Zadeh, M. Rashidi, B. Samali, Comprehensive study of moving load identification on bridge structures using the explicit form of Newmark- β method: Numerical and Experimental Studies, *Remote Sens.* 13 (2021) 2291, <https://doi.org/10.3390/rs13122291>.
- [34] E. Lourens, E. Reynnders, G. De Roeck, G. Lombaert, An augmented Kalman filter for force identification in structural dynamics, *Mech. Syst. Signal. Process.* 27 (2012) 446–460, <https://doi.org/10.1016/j.ymssp.2011.09.025>.
- [35] Y. Mao, X. Guo, Y. Zhao, A state space force identification method based on Markov parameters precise computation and regularization technique, *J. Sound. Vib.* 329 (2010) 3008–3019, <https://doi.org/10.1016/j.jsv.2010.02.012>.
- [36] K. Liu, S.-S. Law, X. Zhu, Y. Xia, Explicit form of an implicit method for inverse force identification, *J. Sound. Vib.* 333 (2014) 730–744, <https://doi.org/10.1016/j.jsv.2013.09.040>.
- [37] M. Ghajari, Z. Sharif-Khodaei, M. Aliabadi, A. Apicella, Identification of impact force for smart composite stiffened panels, *Smart Mater. Struct.* 22 (2013) 085014, <https://doi.org/10.1088/0964-1726/22/8/085014>.
- [38] R. Liu, Z. Hou, S. Wang, D. Sheng, Y. Liu, Dynamic load identification for battery pack bolt based on machine learning. SAE Technical Paper, 2020, <https://doi.org/10.4271/2020-01-0865>.
- [39] J. Zhou, L. Dong, W. Guan, J. Yan, Impact load identification of nonlinear structures using deep recurrent neural network, *Mech. Syst. Signal. Process.* 133 (2019) 106292, <https://doi.org/10.1016/j.ymssp.2019.106292>.
- [40] R. Liu, E. Dobriban, Z. Hou, K. Qian, Dynamic load identification for mechanical systems: A review, *Arch. Computat. Methods Eng.* 29 (2022) 831–863, <https://doi.org/10.1007/s11831-021-09594-7>.
- [41] J. Sanchez, H. Benaroya, Review of force reconstruction techniques, *J. Sound. Vib.* 333 (2014) 2999–3018, <https://doi.org/10.1016/j.jsv.2014.02.025>.
- [42] H. Ouyang, Moving-load dynamic problems: A tutorial (with a brief overview), *Mech. Syst. Signal. Process.* 25 (2011) 2039–2060, <https://doi.org/10.1016/j.ymssp.2010.12.010>.
- [43] E. Jacquelin, A. Bennani, P. Hamelin, Force reconstruction: analysis and regularization of a deconvolution problem, *J. Sound. Vib.* 265 (2003) 81–107, [https://doi.org/10.1016/S0022-460X\(02\)01441-4](https://doi.org/10.1016/S0022-460X(02)01441-4).
- [44] In2Track, Deliverable2.2, Enhanced S&C whole system analysis, design and virtual validation, Chapter 3, Project Shift2Rail, 2019 available online: <https://projects.shift2rail.org/> (access date: 20 January 2022).
- [45] J.J. Kalker, A fast algorithm for the simplified theory of rolling contact, *Vehicle Syst. Dyn.* 11 (1982) 1–13, <https://doi.org/10.1080/00423118208968684>.
- [46] S. Iwnicki, Manchester benchmarks for rail vehicle simulation, *Vehicle Syst. Dyn.* 30 (1998) 295–313, <https://doi.org/10.1080/00423119808969454>.
- [47] R.R. Craig Jr., A.J. Kurdila, *Fundamentals of structural dynamics*, John Wiley & Sons, 2006.
- [48] R. Penrose, in: A generalized inverse for matrices, *Mathematical proceedings of the Cambridge philosophical society*, Cambridge University Press, 1955, pp. 406–413, <https://doi.org/10.1017/S0305004100030401>.
- [49] S.L. Brunton, J.N. Kutz, *Data-driven science and engineering: machine learning, dynamical systems, and control*, Cambridge University Press, Cambridge, 2019, <https://doi.org/10.1017/9781108380690>.
- [50] C. Nagel, F. Ante, M. Putnik, J. Classen, J. Mehner, Characterization of temperature gradients on MEMS acceleration sensors, *Procedia Eng.* 168 (2016) 888–891, <https://doi.org/10.1016/j.proeng.2016.11.298>.
- [51] *Instruction of Procedures at Extreme Weather Conditions RLN00165, Version 002, ProRail, Utrecht, The Netherlands, 2003 in: ProRail (Ed.)*.
- [52] L. Chapman, J. Thornes, Y. Huang, X. Cai, V. Sanderson, S. White, Modelling of rail surface temperatures: a preliminary study, *Theor. Appl. Climatol.* 92 (2008) 121–131, <https://doi.org/10.1007/s00704-007-0313-5>.